PIVOT: A FRAMEWORK FOR MINIMIZING STRESS DEVIATIONS IN STRUCTURAL FORM

A Dissertation

by

NEERAJ YADAV

Submitted to the Office of Graduate and Professional Studies of
Texas A&M University
in partial fulfillment of the requirements for the degree of

DOCTOR OF PHILOSOPHY

Chair of Committee,	Weiling He
Co-Chair of Committee,	Julian H. Kang
Committee Members,	Ergun Akleman
	Zofia K. Rybkowski
	Matthew T. Yarnold
Head of Department,	Gregory A. Luhan

May 2021

Major Subject: Architecture

ABSTRACT

Design of efficient structural members is certainly an intricate process that requires a sound explanation, an exact fit of art and science perhaps, to harness the ever-increasing range of solutions assisted by computational advancements and manufacturing innovations. Many frameworks have been introduced previously to optimize the structural form, however, obtaining a uniform stress distribution has been neglected in favor of determining the least volume satisfying the objective function. Inadvertently, in the process of changing the volume, there are changes to the underlying geometry as well. Since there have been recent studies documenting the impact of geometry on the mechanical performance, it is crucial to obtain reliable knowledge regarding the impact it can have on strategic redistribution of stresses while keeping the volume constant. This investigation proposed the use of Voronoi tessellation, a bioinspired mathematical approach, to determine the positioning of void spaces. Stress-weighted centroids of Voronoi cells were utilized for selecting Voronoi sites based on two different weights. This technique was tested against the Lloyd's algorithm that utilizes geometric centroids to select Voronoi sites. The results demonstrate a statistically significant difference between the Lloyd's algorithm and PIVOT. The proposed approach, with weights inversely proportional to the stresses, showed affirmative signs of convergence while reducing the standard deviation of stress, mean stress and lowering the maximum stress value without making any changes to the volume.

DEDICATION

This work is dedicated to my family.

Maa, for your invaluable sacrifices and love,

Papa, for your unwavering criticism and support,

and Sis, for your friendship.

ACKNOWLEDGEMENTS

I would like to thank Dr. Julian Kang, for providing me the opportunity to pursue this research and the financial support for it, and Dr. Weiling He, for helping me balance the realist borderlines with the idealist nature of this study. I would also like to thank my advisory committee members, Dr. Ergun Akleman for discussions on geometry, Dr. Zofia Rybkowski for her support to help ground this research, and Dr. Matthew Yarnold for his support towards the structural analysis. I want to acknowledge that the guidance, feedback and support by all committee members, throughout the course of this research, was critical in helping shape me this work.

Thanks also goes to the Aggie community especially my friends, colleagues, college faculty and staff for making my time at Texas A&M University a great experience. I would also like to recognize the efforts by Ms. Ginger White, Dr. Stephen Caffey, Dr. Anat Geva, Dr. Wei Yan, Professor Steve Rodgers, and Ms. Elizabeth Smith for their invaluable support over the past few years.

Also, I must state that this work would not have been possible without my family's love, patience and support, and equal credit goes to them for letting me pursue this.

CONTRIBUTORS AND FUNDING SOURCES

Contributors

This work was supervised by a dissertation committee consisting of Dr. Weiling He [chair] of the Department of Architecture, Dr. Julian H. Kang [co-chair] and Dr. Zofia K. Rybkowski of the Department of Construction Science, Dr. Ergun Akleman of the Department of Visualization, and Dr. Matthew T. Yarnold of the Department of Civil and Environmental Engineering. The structural simulations were carried out through Texas A&M University High Performance Research Computing (HPRC) platforms.

All the work conducted for the dissertation was completed by the author independently and the contents of this dissertation are solely the responsibility of the author.

Funding Sources

There are no outside funding contributions to acknowledge related to the research and compilation of this document.

TABLE OF CONTENTS

Page

LIST OF FIGURES

Page

LIST OF TABLES

Page

CHAPTER I

INTRODUCTION

This dissertation will chart the field analyzing the structural form in the context of uniform stress distribution and light-weighting, that is, removing unfavorable dead loads which are primarily due to the self-weight of the structure. Among any loads acting on a structural member, dead loads are considered as the static forces acting for an extended period of time compared to the life span of the structure. Hence, from structural efficiency perspective, the absence of any unfavorable self-weight is preferred, and this study focuses on such optimization as related to the recent manufacturing methods and trends in construction.

I.1 Light-weighting

Construction has been going on since the advent of civilization and is often considered as a reflection of the building technology of the period. Early construction assemblies, from the post and lintel system of the Stonehenge, United Kingdom to renaissance structures such as Brunelleschi's double dome of the Cathedral de Santa Maria, Florence, Italy effectively display the unique structural innovations of the past. Primarily, for all structural load-bearing purposes, the central theme in such projects was the use of solid cross-section members by the architects and engineers. Such structural members will be referred to as the Level Zero of light-weighting for the rest of this investigation.

Any instance where no change has been made to the members' cross-section for structural purpose would be placed at this level. This makes Level Zero members particularly useful as compression members, and highly desirable for projects where the structure is to be constructed by stacking members. However, if the span of the members is to be increased, their self-weight would increase three-fold, once for the length and twice for the cross-section, thereby limiting the applications. A sample Level Zero light-weighting member is shown in Figure 1.

Figure 1 Level Zero of light-weighting with a solid rectangular cross-section.

Advancements in the classical theory of mechanics of materials and the onset of industrial production, about three centuries ago, helped reposition the material to strategically important areas within the member. As a result, the cross-

section of these structural members changed significantly from a solid rectangular or circular outline as discussed by Rozvany and Zhou (1991).

While Level Zero members can still be found in use today, architects and engineers have a wider availability of enhanced solutions with cross-sections such as I, H, C, L and S being some of the predominant ones as noted by Bank and Bednarczyk (1988). A typical Level One light-weighting member with I cross-section is shown in Figure 2.

Figure 2 A structural member equivalent to the Level One of light-weighting.

The beam or a truss or frame design can be considered as the essential element of a structural system. Trusses avoid shear and bending in the structural members and have different boundary conditions than rigid frame systems. This study will be limited to the beam in attempt to comprehend the fundamentals.

When a beam is loaded by forces or couples, stresses and strains are developed throughout the interior of the beam. These stresses and strains can be determined after finding out the internal forces and internal couples that act on the cross-sections of the beam. A free-body diagram of a simply supported beam with a Point Load at the top is shown in Figure 3 along with the stress and strain diagrams at the cross-section.

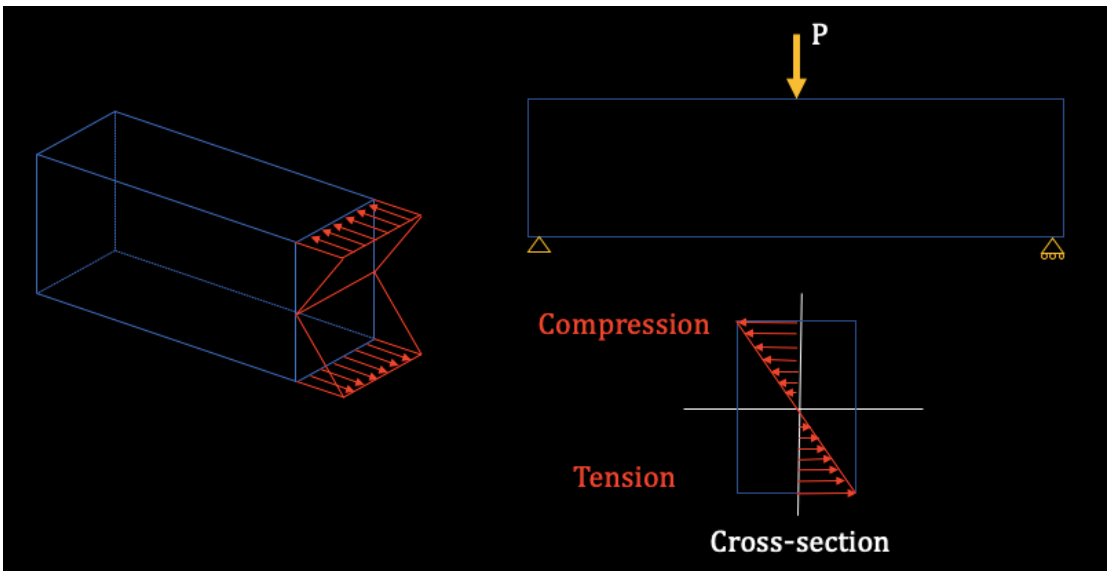

Figure 3 Mechanics of a simply supported beam.

The design space is divided into equal units where vector forces act on point coordinates and the net impact on a body is determined using the free-body diagrams and the conditions for equilibrium behavior. If the material was repositioned across the beam's cross-section to replicate the structural diagrams, it would result in the placement of a majority of the material at the end such that it

gradually decreases to zero at the midpoint before increasing to maximum amplitude again at the other end. Since it would not be a single piece if the midpoint was reduced to zero, providing a standard thickness through the middle cross-section and a wider placement at the ends is reasonable for practicality. This would result in a cross-section similar to the I or H beam. Such structural members fall under the family of Level One of light-weighting along with additional examples such as C, L and S among others. These members are widely used on construction jobsites today and are readily available in a variety of standard sizes. The initial success of these structural members was made possible by the manufacturing and production advancements of the industrial age.

One of the earliest examples of the industrial production upending the building technology was displayed by the Crystal Palace in 1851 for the World Trade Exhibition as noted by Addis (2006). It efficiently summarized the advantages offered by offsite manufacturing, modularity and innovations of construction methods brought forward by the industrial revolution. For instance, the wall thickness of the cast-iron columns was adjusted by varying the diameter of the inner cavity to carry the anticipated structural loads while retaining the external modular functions. Similarly, the development of Portland Cement in early 20th century marked innovations such as the monolithic construction of two-storied buildings as ideated by Edison (1917).

3D printing has effectively demonstrated the capability and potential to revolutionize the 21st century, and the pace of innovation in manufacturing and

computational resources has accelerated in the past two decades. While these advancements have already impacted the aerospace, automotive and biomedical fields among others, they have also made significant foray into the architecture and construction industries. Full-scale structures are already being realized with major success, such as the robotic cement-based 3D printing with sparse infill as mentioned by Nematollahi et al. (2017) and the lightweight 3D printed bridge by MX3D (2018).

In addition, the scientific community is certainly better equipped now to uncover the fundamentals of morphogenesis. The recent progress, unraveling the workings of Nature along with the studies on the underlying role of geometry in physical properties, is being taken into account during the design phase. However, this idea has been around for centuries. For instance, in 1600s Galilei Galileo speculated on the bone size and their corresponding strength for different animals as noted in Martin (2007). Meanwhile, Thompson (1917) while exploring the structure of bone in *On Growth and Form* states that Nature strengthens the bone in precisely the manner and direction in which the strength is required.

More recent studies, with help of computerized tomography (CT) scans, have pointed that the impact of increase in length of bones do not necessarily leads to increase in mechanical strength. Such gains are usually offset and even significantly lost due to self-weight of the additional length similar to the challenges displayed by the structural members. However, different bones have significantly different internal porosity, and this is evident across many species according to

the study by Ryan and Walker (2010). Another study by Sullivan et al. (2017) evaluated the cross-section of the avian bones, some of the extreme lightweight structures, and discussed the variations in profile and porosity along the length.

The advantages offered by bone inspired microarchitectures to achieve enhanced fatigue life is now being realized in studies such as the one carried out by Torres et al. (2019). In another significant study by Audibert et al. (2018), an additively manufactured beam, based on isostatic stress lines, was compared with two bioinspired beams with cavities based on the avian bones and terrestrial bones. The terrestrial bone-inspired beam significantly outperformed the other two. These 2.5D beams, manufactured with stainless steel using selective layer melting (SLM), are shown in Figure 4. This and the rest of the previously published images included in this dissertation are borrowed under the provisions of Fair Use.

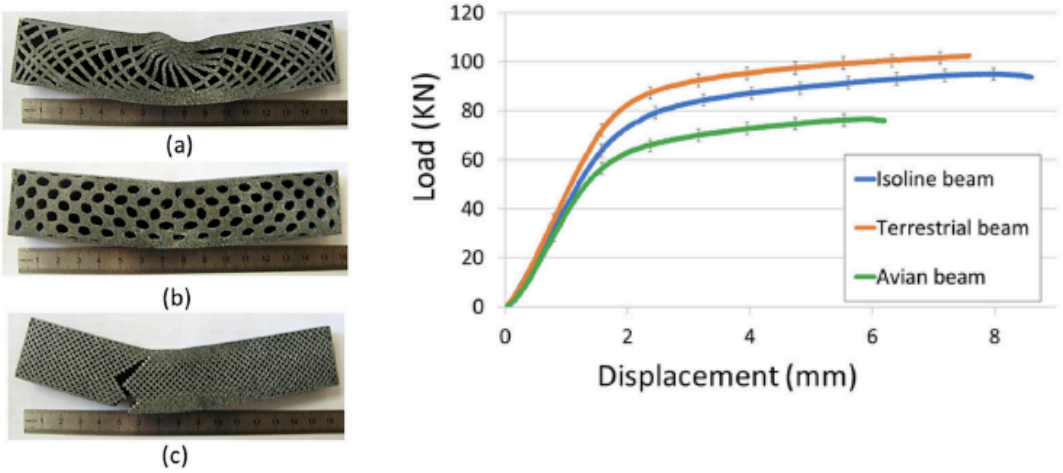

Figure 4 A study by Audibert et al. (2018) comparing structural performance of bone-inspired beams with the isoline beam.

While the understanding of mechanics is still evolving, the technology to realize complex structures is now at disposal. It has provided a tremendous support to the possibility of further enhancing the structural members for a strategic rather than a singular and uniform cross-section. The aforementioned bio-inspired forms are made possible by the developments in manufacturing sector. Most prominently, the feasibility and accessibility of techniques such as additive manufacturing including extrusion-based methods, particle bed-based additive manufacturing, and robotic fabrication among others, as noted by Al Rashid et al. (2020), has played a pivotal role in this advancement.

In addition, studies are being carried out to specifically identify design criteria for additive manufacturing such as the one by Plocher and Panesar (2019). As noted in Figure 5, there are certain extrinsic parameters that are crucial for each specific target.

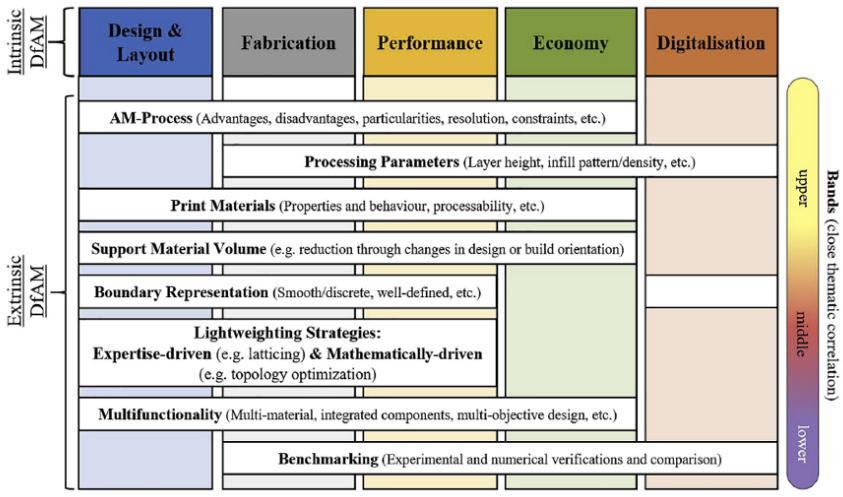

Figure 5 An overview of Design for Additive Manufacturing as noted by Plocher and Panesar (2019).

The commercialization of a technology greatly impacts its economic viability, however, factors such as the Design & Layout, Fabrication, Performance, and Digitization are more technical factors that do not overlap with the economy. Hence, for a study that is independent of the economic factor, the focus shifts solely to the *Boundary Representation* and *Lightweighting Strategies*, a review of which is provided in the next chapter.

While the exact theory of mechanics is still evolving, important adjustments and manufacturing realizations have been made over the past two decades. As a result of these innovations, Level Two of light-weighting is considered reached for the purposes of this study as depicted in Figure 6. The Level Two member, shown on the extreme right, is used to illustrate the conceptual leap from Level One, shown in the center.

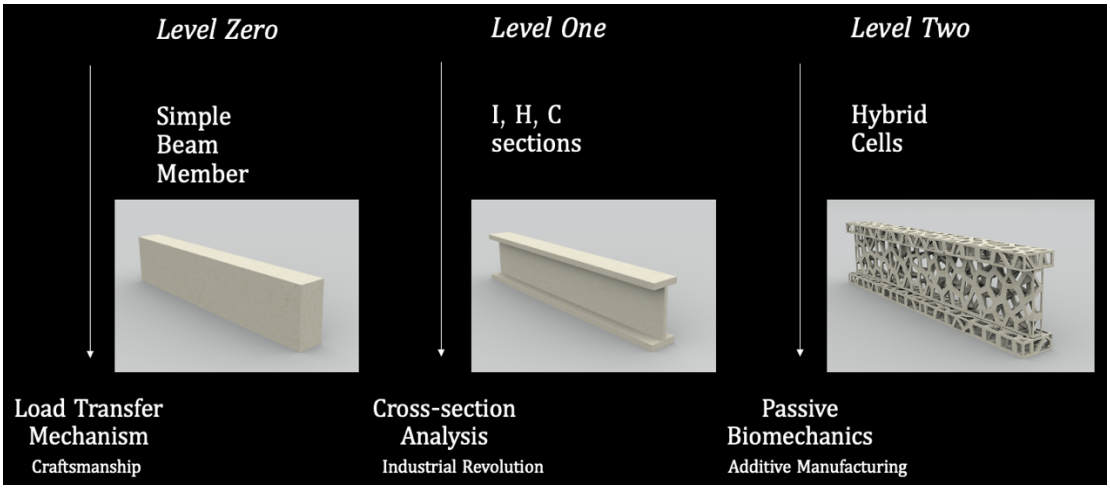

Figure 6 Light-weighting Levels for optimization of structural members.

It is certainly possible that the profile of the Level Two member can also vary significantly along the length depending on the loading and boundary conditions. Hence, the external form will also have variations in addition to the internal cellular tessellations. Also, the current mechanics theory for Level Two light-weighting is referred to as Passive Biomechanics since a majority of the present efforts are limited to replicating the forms found in Nature. However, most biological elements evolve and change their forms over their lifetime, thus resulting in what could be considered as active biomechanics. A better understanding of the underlying principles and further control of material behavior has the potential to transform into the Level Three of light-weighting. This dissertation will only explore the structural form in relation to the Level Two of light-weighting.

I.2 Motivation

Design of efficient structural members is certainly a major challenge and light-weighting, that is, weight reduction without impacting the structural performance and, as a result, minimizing any forces or moments acting on the member due to self-weight, plays a prominent role in it. However, light-weighting also concerns the strategic redistribution of weight in order to avoid unintended stress variance arising from the material placement.

A successful light-weighting solution is of prominence because of several reasons. Firstly, it would allow the structural members to carry out their functions

efficiently while iteratively making modifications to the geometric form until the form follows the function, that is in this case, the structural function. This has significant ramifications in the design and construction of support-free long span structural members while distributing the stresses uniformly.

Secondly, it is important because this will result in a more efficient use of materials and therefore be helpful for the ecology. In addition, it will also enrich the intellectual efforts in design, and the diversity in built environment by seeking to utilize bioinspired generative design to optimize for structural performance.

I.3 Research Question

While Level Two light-weighting is providing significant structural improvements just as Level One light-weighting did, can we utilize Level Two light-weighting such that all internal structural members develop same amount of stress without making any changes to the volume (weight) and the external boundaries?

CHAPTER II

STATE OF THE ART

Typically, the structural optimization problem is regarded as the means to reduce the weight by reducing the volume for a given set of bounding conditions and loading conditions. Numerical explorations in such optimization problems usually involve either cantilever, half Mersserschimstt-Bölkow-Blohm (MBB) beam or full MBB beam. However, there is no explicit agreement by the scientific community on their aspect ratio making the comparisons difficult.

II.1 Topology Optimization

One of the earliest publications regarding volume optimization was put forward by Michell (1904). This illustration in Figure 7 was to determine the minimum volume required by the beam AB for a Force F acting at center C.

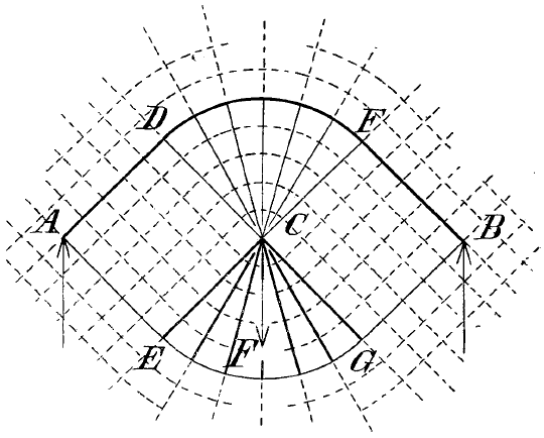

Figure 7 Least volume of material for a beam loaded at the center as presented by Michell (1904).

A free body diagram at C would have to balance the moments caused by the support reactions acting at ends A and B. Hence, a circular radius of CD (same as CE, CF and CG) can be identified to counter the moments generated by the reaction forces at the ends depending on their distance from C. This will eventually culminate in what was presented as the least volume of the material required for this problem, as defined by the ADFBGEA outline.

It provided the foundation for layout optimization which was carried forward by Rozvany (1972). Around that time, the optimality criteria algorithm was introduced by Prager and Taylor (1968) aiding the formulation of the 99-line MATLAB work by Sigmund (2001) as displayed in the Figure 8.

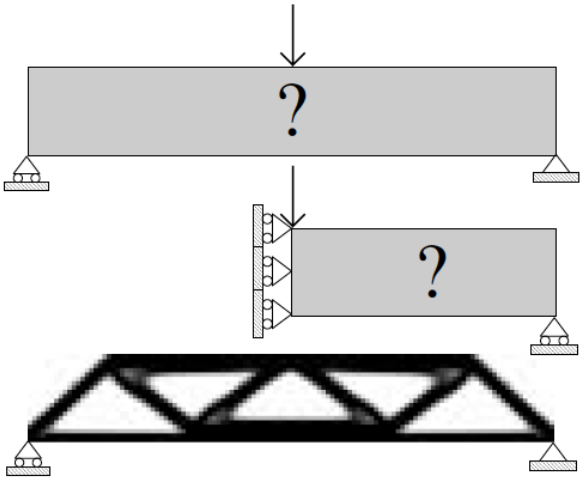

Figure 8 Topology optimization of a full MBB beam as demonstrated by Sigmund (2001).

Meanwhile, a convex linearization (CONLIN) method was introduced by Fleury and Braibant (1986). Prior to that, the conventional linearization replaced

the primary problem with a series of linear programming problems and could only converge when the optimal solution was at the vertex of the feasible domain. The case for adding artificial side constraints which were called move limits to gradually tighten the feasible domain was speculated to overcome this severe limitation. However, the convex curvature approximation function presented by the authors did not require such limits because a convex and separable subproblem, through the utilization of the first-order Taylor series expansion, automatically ensured separability as shown in Figure 9.

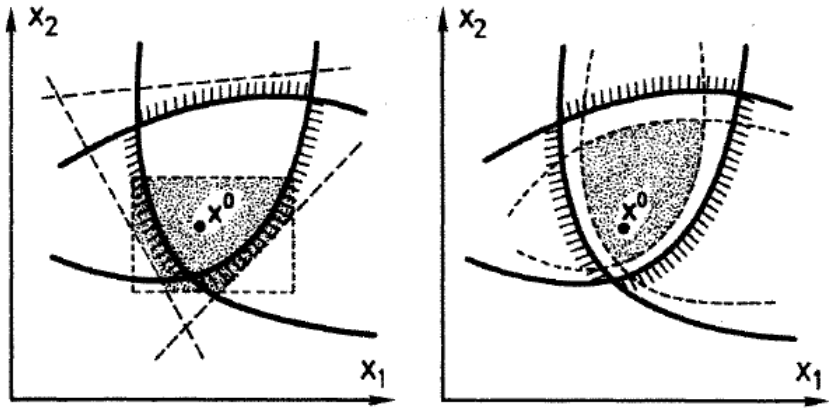

Figure 9 Optimization through conventional (left) and convex (right) linearization as illustrated by Fleury and Braibant (1986).

An enhanced version of CONLIN was introduced by Svanberg (1987) as method of moving asymptotes (MMA). It controlled the subproblems with the flexibility of moving asymptotes, thereby speeding up the convergence process in many instances. This technique forms the foundation for many of the present-day structural optimization explorations.

The homogenization method with isotropic material assumption was introduced by Bendsøe and Kikuchi (1988) and later modified to the solid isotropic method with penalization (SIMP) by Bendsøe (1989) and Zhou and Rozvany (1991). It utilized the means to obtain the density gradient. Meanwhile, Eschenauer et al. (1994) introduced the topological derivatives, also known as 'bubble method', shown in Figure 10. It is a special case of homogenization where the topological derivatives represent the density going to 0 (void).

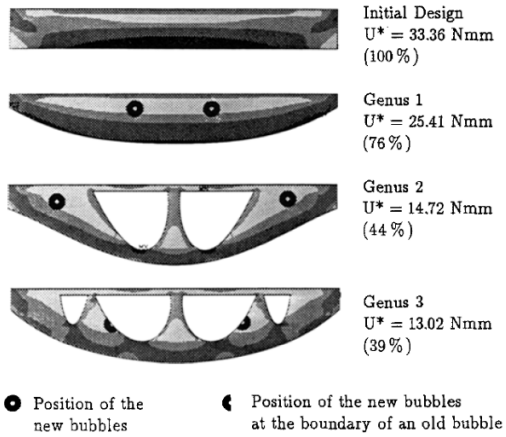

Figure 10 Topology optimization of a panel rib fixed at the top ends and uniformly loaded on top using the bubble method.

This can also be used together with other techniques such as the level set approach or directly in element-based update as demonstrated by Allaire et al. (1997) and Burger et al. (2004). The level set models define the boundary as the zero level (contour) of a mathematical function such as energy of deformation or stress developed. It was introduced by Osher and Sethian (1988) to utilize an implicit moving boundary.

Meanwhile, phase method which works at the interface of a transition such as solid-liquid transitions, was introduced by Bourdin and Chambolle (2006). In addition, there are discrete methods where formulating the functions in discrete variables is reasonable, however, the mathematical solution for sensitivity analysis can be challenging. Notable ones are evolutionary structural optimization (ESO) by Zhou and Rozvany (2001), and bidirectional evolutionary structural optimization (BESO) by Querin et al. (1998). Notable combined techniques (density and discrete) are extended finites element method (xFEM) by Van Miegroet and Duysinx (2007) and the deformable simplicial complex (DSC) as presented by Misztal and Bærentzen (2012).

Application of topology optimization to perforated I-sections have also been carried out such as the study by Tsavdaridis et al. (2015). Meanwhile, neural network-based formula was used by Abambres et al. (2019) to evaluate the buckling loads for I-section cellular steel beam. In another study by Huber (2018) a feed forward artificial neural network was exploited to predict fundamental mechanical properties like Young's modulus, yield strength, and Poisson's ratio based on the cut fraction (or average coordination number).

One study by Zhang et al. (2018) presented an approach to optimize topology of internal stiffeners based on the growth mechanism of biological branch system in Nature. The internal stiffeners grow, bifurcate and degenerate towards the direction of maximum overall structural stiffness. Another study by Molotnikov et al. (2019) about architectured polymeric materials using additive manufacturing

also noted exiting results. Additionally, improvements in formulations have also provided the opportunity to introduce design dependent boundary conditions for topology optimization using density gradient technique as presented by Wang and Qian (2020).

Another study from a different group, led by Wang et al. (2020), presented topology optimization for structural layout and robotic fabrication sequence using the SIMP technique as shown in Figure 11. It included the compliance due to the weight of the robotic arm such that the intermediate structure is able to support its load. The color bands represent the time-field and position of the robot.

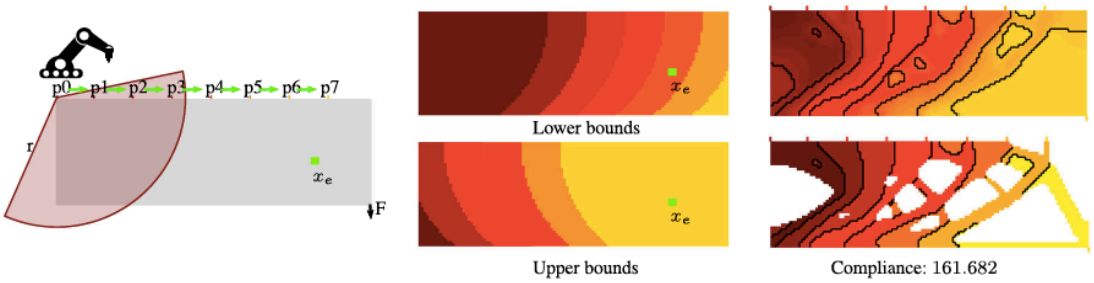

Figure 11 Structural layout and fabrication sequence optimization approach by Wang et al. (2020).

II.2 Cellular Optimization

The structural optimization progress has accelerated to new heights especially because of the accessibility of additive manufacturing in the last decade. Increasing amount of solutions are geared towards cellular structures due to the 3D printing advantages they present. This section canvasses both periodic arrangement of cells as well as unstructured arrangements.

Wu et al. (2016) presented adaptively refined lattice structure for topology optimization while an upper bound for localized material volume was introduced to obtain bone-like porous infill for additive manufacturing by Wu et al. (2017). Meanwhile, Wu et al. (2019) presented an approach inspired by natural cellular materials to conform with the principle stress direction and the boundary of the optimized shape to assist the manufacturing as shown in Figure 12.

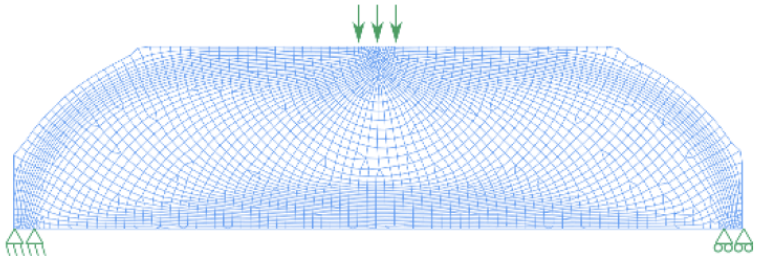

Figure 12 Optimized 2D lattice beam with spatial variations in orientation, porosity and anisotropy as presented by Wu et al. (2019).

Panesar et al. (2018) also investigated the performance of additively manufactured implicit surface-based cells using the SIMP framework. Zhong et al. (2019) tested the mechanical properties of lightweighting using periodic stainless-steel lattice structures fabricated using SLM. Additional work has been carried out to determine infeasible print angles and carry out relevant post processing for additive manufacturing such as Leary et al. (2014), where digitally print-ready design is being explored by Iso-XFEM (Isoline-Extended Finite Element Method). Lattice structures have also been utilized to reduce the vibrations as demonstrated in Ramadani et al. (2018).

Meanwhile, Al-Ketan et al. (2018) compared various geometries and noted that the triply periodic minimal surfaces outperformed strut-based structures, and that the effect of geometry on mechanical properties is more pronounced at decreased volume fractions. Another study by Li et al. (2018) tested gyroid based functionally graded periodic arrangement for additive manufacturing. Also explored is the topology optimization of periodic microstructure modulated and oriented through changes in the homogenization formulation for lattice structure applications by Allaire et al. (2019).

Since structural optimization and topology optimization is a very broad field, additional well consolidated literature reviews are available in the public domain including recent studies comparing various optimization techniques to include the advancements offered by additive manufacturing as noted in Feng et al. (2018), Tyflopoulos et al. (2018), and Liu et al. (2018).

On the unstructured arrangement forefront, recent research has shown that cellular irregularity based on Voronoi tessellation in porous scaffold for orthopedic reconstruction can significantly impacts its mechanical behavior as noted by Wang et al. (2018), Du et al. (2019), and Du et al. (2020). Also noted are the similarities between the performance outcomes from Voronoi tessellation to the human bone structure.

The Voronoi tessellation is a mathematical concept that partitions the space into regions of influence depending on their distance from the point sites, as displayed in Figure 13.

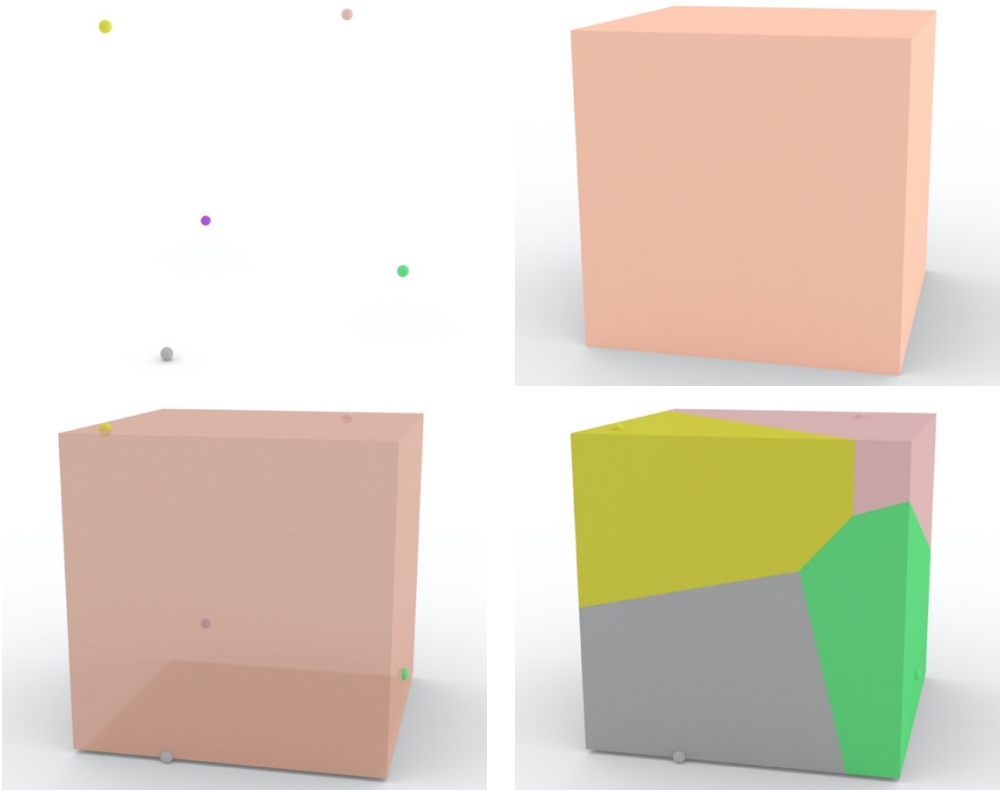

Figure 13 Generation of Voronoi tessellation from five sites bounded in a cubic domain.

Descartes (1644) illustrated a theory in third part of his *Principia Philosophiae*, to demonstrate the universe as set of (weighted) regions around each star-*the heavens* as shown in Figure 14. This was one of the earliest depictions of partitioning space based on their distances from key sites of interest. However, it was much later in 1850 that Peter Gustav Lejeune Dirichlet provided a mathematical formulation on influence of point p on another point q for $\mathbb{R}2$ and $\mathbb{R}3$ vector space as noted in Ash and Bolker (1985). Eventually, Voronoi (1908) provided the formulation for $\mathbb{R}n$ vector space. For their contributions, it is also called Dirichlet tessellation or Voronoi diagrams among other names.

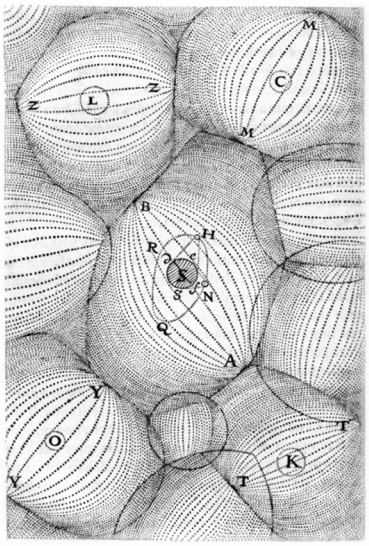

Figure 14 Vortices diagram as illustrated by Descartes (1644) in *Principia Philosophiae*.

This concept will be referred as Voronoi tessellation in the rest of this document. A graph-theoretical dual to Voronoi tessellation is called Delaunay triangulation and was formulated by Delaunay (1934). Additional conceptual details and background of the Voronoi tessellation can be found in Pokojski and Pokojska (2018).

With regards to structural analysis, Voronoi tessellation was used by Ghosh (2011), and Gain et al. (2015) to generate Finite Element Analysis mesh. A few significant studies have previously attempted to utilize Voronoi tessellation to impact the performance of the resulting form. Lee et al. (2018) developed an approach for support free hollowing for additive fabrication using Voronoi tessellation of ellipses. The study made improvements over a previous attempt but could not achieve a global uniform stress distribution as seen in Figure 15.

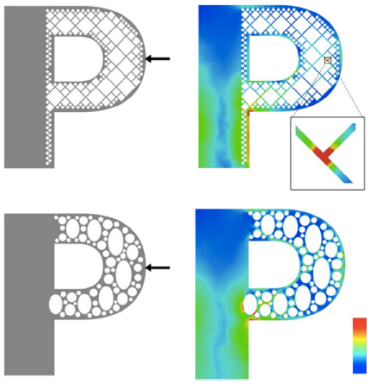

Figure 15 Comparison between Wu et al. (2016) (top) and Lee et al. (2018) (bottom) for fabrication-related adaptively refined hollowing.

One of the earliest notable research in relation to Voronoi tessellation was carried out by Allaire and Schoenauer (2007) where an evolutionary algorithm was adopted to determine the optimal structures. Shown in Figure 16 is a 2D cantilever beam. The solution proposed a pixel (or voxel) grid where volume (weight) constraints and structural performance were evaluated to determine the acceptance or rejection of the polygon (or polyhedron) to determine the optimal structure and identifying next generation of Voronoi sites.

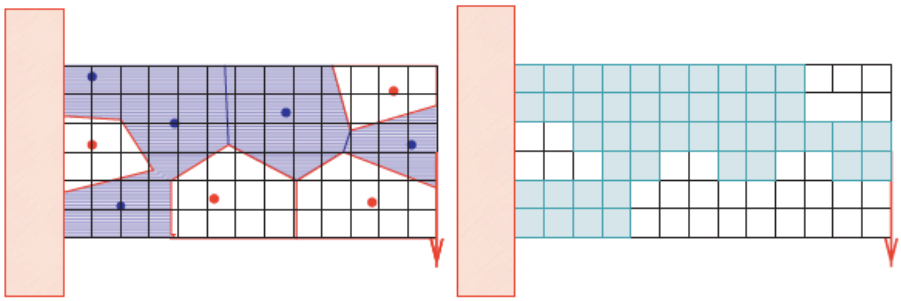

Figure 16 Cantilever beam optimization using Voronoi sites in a voxel grid as presented by Allaire and Schoenauer (2007).

While that approach relied upon the presence or absence of the whole Voronoi cell, a remarkable shift is noted in the attempt by Martínez et al. (2016). A density field is utilized, and every single point is queried in the design space based on the refinement level. The Voronoi edges were eventually turned into volumetric entities in a remarkable approach for 2D as well as 3D structures.

The objective of the research was directed towards developing procedural Voronoi forms for additive manufacturing. The flexibility of the resulting outcomes is controlled by varying the density field as shown in the Figure 17. This study noted that the approach could not enforce convexity at the boundary but the use of convex cells of Voronoi tessellation are otherwise well suited. The research scope did not include any structural optimization but was rather focused on manipulating the rigidity of the resulting forms.

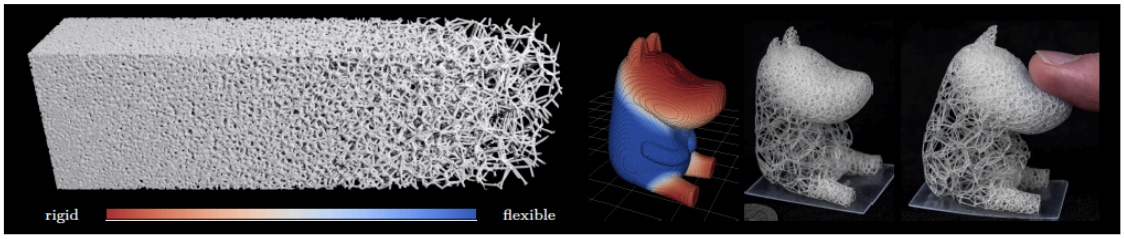

Figure 17 Density gradient based approach to alter rigidity of additively manufactured Voronoi tessellation as adopted from Martínez et al. (2016).

Further research has been carried out more recently by Martínez et al. (2018) to control for fabrication direction by manipulating angles parameters, Voronoi site density and distance. This is illustrated in Figure 18.

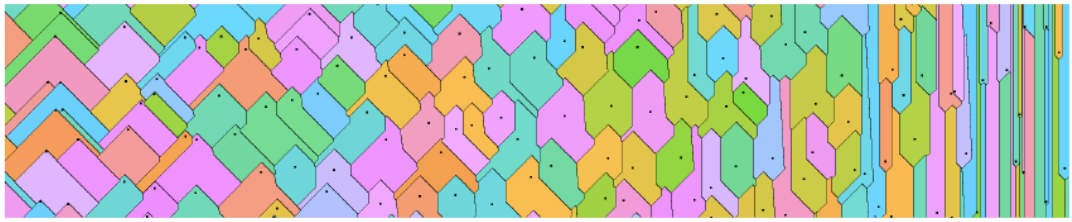

Figure 18 Varying the orientation of Voronoi tessellation for enhanced fabrication as presented by Martínez et al. (2018).

Additional research has also been conducted to alter the young's modulus and Poisson's ratio by Martínez et al. (2019), and Gao et al. (2019). An attempt at utilizing Voronoi tessellation for structural enhancement has also been carried by Cucinotta et al. (2019) as shown in Figure 19. The initial solution is prepared from a surface grid of points as Voronoi tessellation sites.

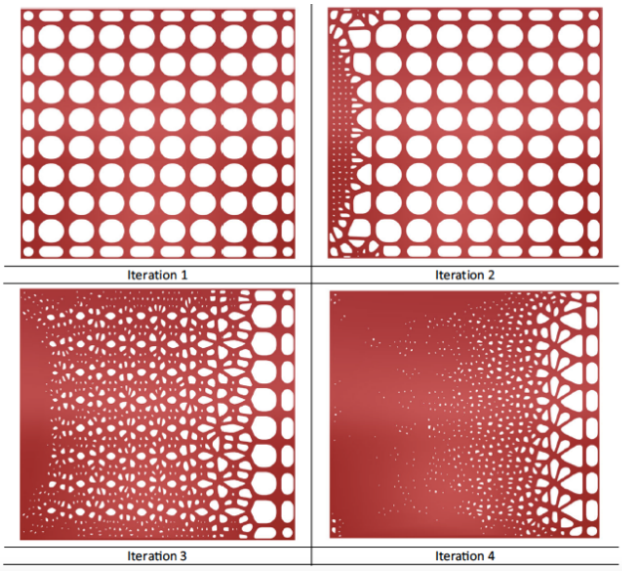

Figure 19 An approach by Cucinotta et al. (2019) to optimize structural performance by dynamically varying the count of Voronoi sites on a surface.

The edges are thickened, and inner material is hollowed out and intersection is filleted with a fitting radius to avoid angular points. Upon obtaining the stresses, more points are added iteratively in regions with high stresses. Meanwhile, the points where the hollowing perimeter is below a threshold, hollowing is not triggered. Hence, if a region fails to meet the allowable stresses, it will keep seeing an increase in the number of control points till they are too tightly packed that hollowing condition is discarded.

Meanwhile, Lu et al. (2014) carried out an interesting study to improve the strength to weight ratio by utilizing a stress-based iterative Voronoi tessellation. This approach computed an initial stress map for the given form, under predefined boundary and loading conditions, and is used to generate the corresponding interior Voronoi sites. The population is propagated such that there is a higher dispersion at regions with high stresses before incorporating the Centroidal Voronoi Tessellation (CVT), introduced by Lloyd (1982) and as summarized in Du et al. (1999) to achieve results similar to an error diffusion process analogous halftoning. Rest of this text will refer it as the Lloyd's algorithm.

In addition, the porous extraction is carried out by a hollowing parameter expressing an iso-value in the harmonic field for each cell. The optimization is carried in a two-loop process where the inner loop iterates till all the hollowing value for each cell is below the yielding point. The outer loop reduces the number of cells by merging regions with similar hollowing parameter and replacing them with a single site and the same value. The inner loop is again refined to

accommodate for the change in the Voronoi structure and the algorithm continues till convergence is reached or due to the failure in change of the overall volume between successive iterations. This process is depicted in Figure 20.

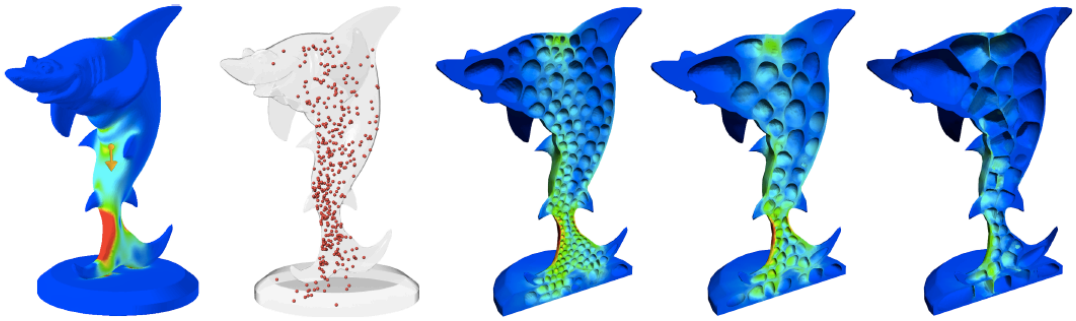

Figure 20 Overview of the approach adopted by Lu et al. (2014).

The authors noted that it was sufficient to begin with 100 unique sites in most cases. These sites were introduced at high stress regions, and their positions were subsequently altered by applying the Lloyd's algorithm before reducing their count till the determination of the lightest weight needed to meet the loading requirements was achieved.

II.3 Limitations

A majority of the methods have been explored in prior literature to optimize the structural form based on the strain energy, optimal layout, fundamental frequencies and lately for fabrication efficiencies and their combinations. However, obtaining a uniform stress distribution has been neglected in favor of determining the least volume satisfying the objective function.

Application of topology optimization to perforated I-sections has been carried out by Tsavdaridis et al. (2015) as shown in Figure 21. It is one of the few studies that attempted to reduce the variance of stress across the members but could not completely achieve that objective as noted by the authors.

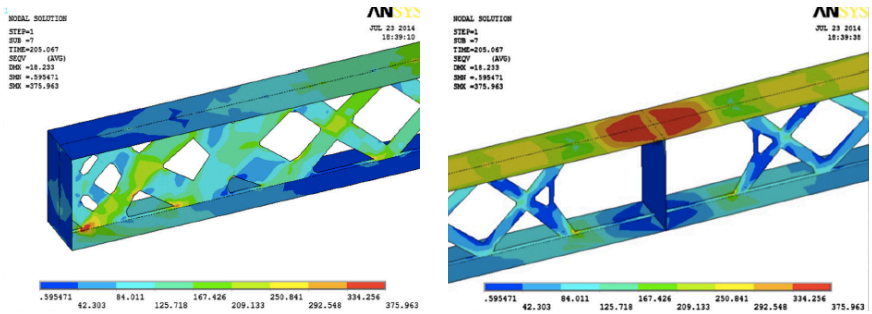

Figure 21 Attempt to obtain uniform stress distribution utilizing Level Two light-weighting of I cross-section beam by Tsavdaridis et al. (2015).

Recently Picelli et al. (2018) presented an approach to utilize the level set method for stress minimization. Shown in Figure 22 is the compliance minimization solution and the stress minimization solution for a beam notch model, but the no specific attempts were made to reduce the stress deviations.

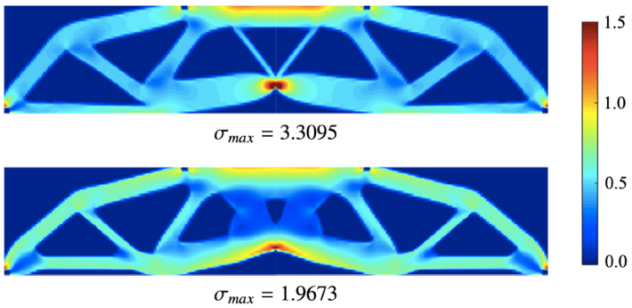

Figure 22 Level set optimization by Picelli et al. (2018) for compliance (top) and stress minimization (bottom).

A majority of the solutions that rely on density-based techniques, are generally able to obtain achieve a mathematically lightweight solution. However, the conversion of this gray scale model to define exact *Boundary Representation* is often challenging. Additionally, many other techniques such as SIMP are nonconvex and mesh dependent. Also, inadvertently in the process of changing the volume (weight), a majority of the techniques make changes to the underlying geometry as well. Since there have been recent studies documenting the impact of geometry on the mechanical performance, especially at higher porosity, it is crucial to obtain reliable knowledge regarding the impact it can have on strategic redistribution of stresses while keeping the volume constant.

In case of periodic arrangements, many specific structures have been explored but a single function to generate a multitude of cellular structures is missing in most of the studies. This implies that every periodic cellular lattice will have to be individually evaluated making it a cumbersome trial and error process instead of a more organized and efficient approach.

Meanwhile, the study by Audibert et al. (2018), successfully utilized Level Two light-weighting to demonstrate that our classical understanding of mechanics is not conclusive, and presented that it could be outperformed by bioinspired cellular structures. However, as seen in the Figure 23, there were significant regions with non-uniform distribution of stresses in the isoline beam structures as well as the two bio-inspired cellular beam structures.

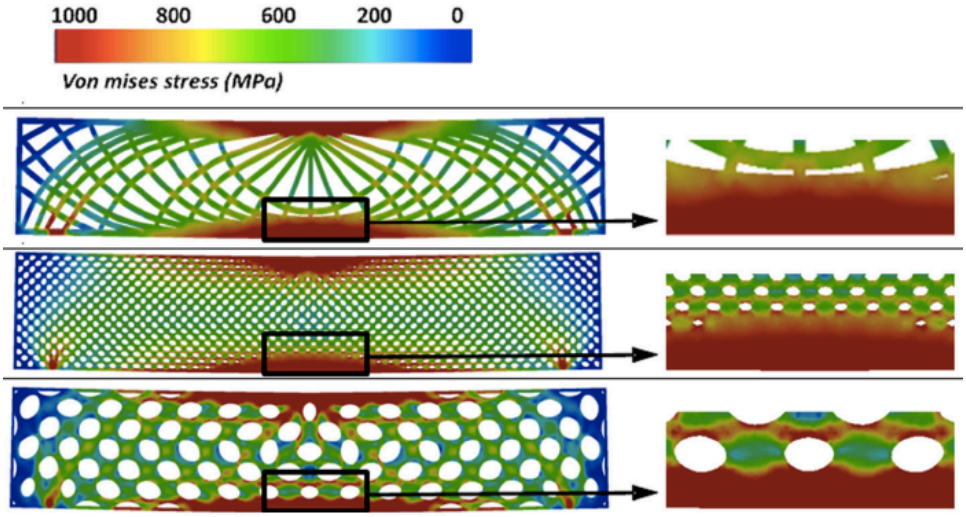

Figure 23 Uneven stress concentrations noted in the study by Audibert et al. (2018).

The ability of the Voronoi tessellation to generate a multitude of cellular arrangements by varying the position of the Voronoi sites has been utilized lately. However, a majority of them have been related to the interior hollowing for additive manufacturing purposes or to alter the mechanical properties such as flexibility.

One notable study by Lu et al. (2014) attempted to incorporate the stress outputs in altering the Voronoi tessellation based internal geometry and iteratively merged cells with similar harmonic stress values. While the results achieved by this method were very impressive, due to the computational challenges involved, the study did not conduct structural simulations and the results are based on approximate computations. Meanwhile, the other attempt by Cucinotta et al. (2019) was limited to the generation of Voronoi sites on a surface.

Also, while some other studies have attempted to vary the density of the Voronoi sites to evaluate their impact on structural and mechanical properties, a

sound explanation to corelate the two seems to be lacking. The Lloyd's algorithm is often utilized for its error diffusion properties but given that the Voronoi Tessellation and Lloyd's algorithm are mathematical concepts, incorporating them to enhance structural performance without any fine-tuning for the objective is bound to have limitations.

Design of efficient structure requires a sound explanation to harness the ever-increasing range of solutions assisted by computational advancements and manufacturing innovations. Also, structural optimization and light-weighting attempts by volume reduction have dominated the academic pursuits in the last century while improving the structural performance by minimizing the stress variance has been neglected for no tangible reason. Moreover, the quest for a bioinspired principle of order to regulate and coordinate the positioning of vacuum and material guided this investigation.

CHAPTER III

PARAMETRIC INSITU VORONOI

As stated earlier, the Voronoi Tessellation and the Lloyd's algorithm are powerful mathematical concepts that can generate a huge amount of periodic as well as unstructured arrangements by altering the position of their Voronoi sites. However, incorporating them to enhance structural performance without any fine-tuning for the objective is bound to have limitations.

This investigation was primarily concerned with determining methods to parametrically vary the position of the Voronoi sites in order to enhance the structural performance and achieve uniform stress distribution. In order to determine the relationship between them, the Voronoi tessellation can be primarily altered in three ways. First, by addition or removal of Voronoi sites iteratively as defined by a relation with the stresses developed. This method was utilized by Lu et al. (2014), and Cucinotta et al. (2019). Second method is to keep the number of Voronoi sites constant throughout while changing their positions based on a relationship with the stresses developed in the cells. Third method is to keep the number of Voronoi sites, and their positions fixed while altering the growth rate based on the stresses in the region. However, the output from the third method would highly depend on the count of sites and their position to begin with. Since there were no published studies regarding that, at the time of this investigation, it was reasonably determined to proceed with the second method.

The count of Voronoi sites was to be kept fixed while their position coordinates were to be parametrically varied depending on the structural behavior after each iteration. However, another issue before proceeding forward was to determine the ability to create lightweight member with controllable porosity. The Voronoi tessellation partitions space into regions of influence but it does not provide a roadmap to define a manifold surface corresponding to the Voronoi cell besides the cell boundary itself. Similarly, the parametrically stress-weighted Voronoi tessellation can help identify new Voronoi sites but defining porous volumetric representation of a Voronoi cell is as much a geometry computation as it is an architectural style.

III.1 Porous Scaffold

A few significant approaches have been recorded so far for the *Boundary Representation* of porous Voronoi cells. A common theme among such solutions were the attempts to convert the edges of the cells to volumetric 2-manifold surface, thereby ensuring that the Voronoi site of the cell embodies the void. Such thickening of the edges will be referred to as the scaffold of a Voronoi cell for the purposes of this text.

Three scaffold instances, found in the literature, are discussed here along with the introduction of a novel scaffold for the thickening of the edges of the same Voronoi tessellation. The illustrations were carried out on *Rhinoceros 7* by McNeel (2015) and *Grasshopper3D* by Rutten (2015).

The first approach, Cylindrical scaffold, is depicted in Figure 24. In this attempt, all the curve that constitute the edges of the Voronoi cells are thickened as cylindrical pipes with a designated radius τ. The ends of these pipes could be round capped with a half sphere of radius τ or otherwise can be left flat.

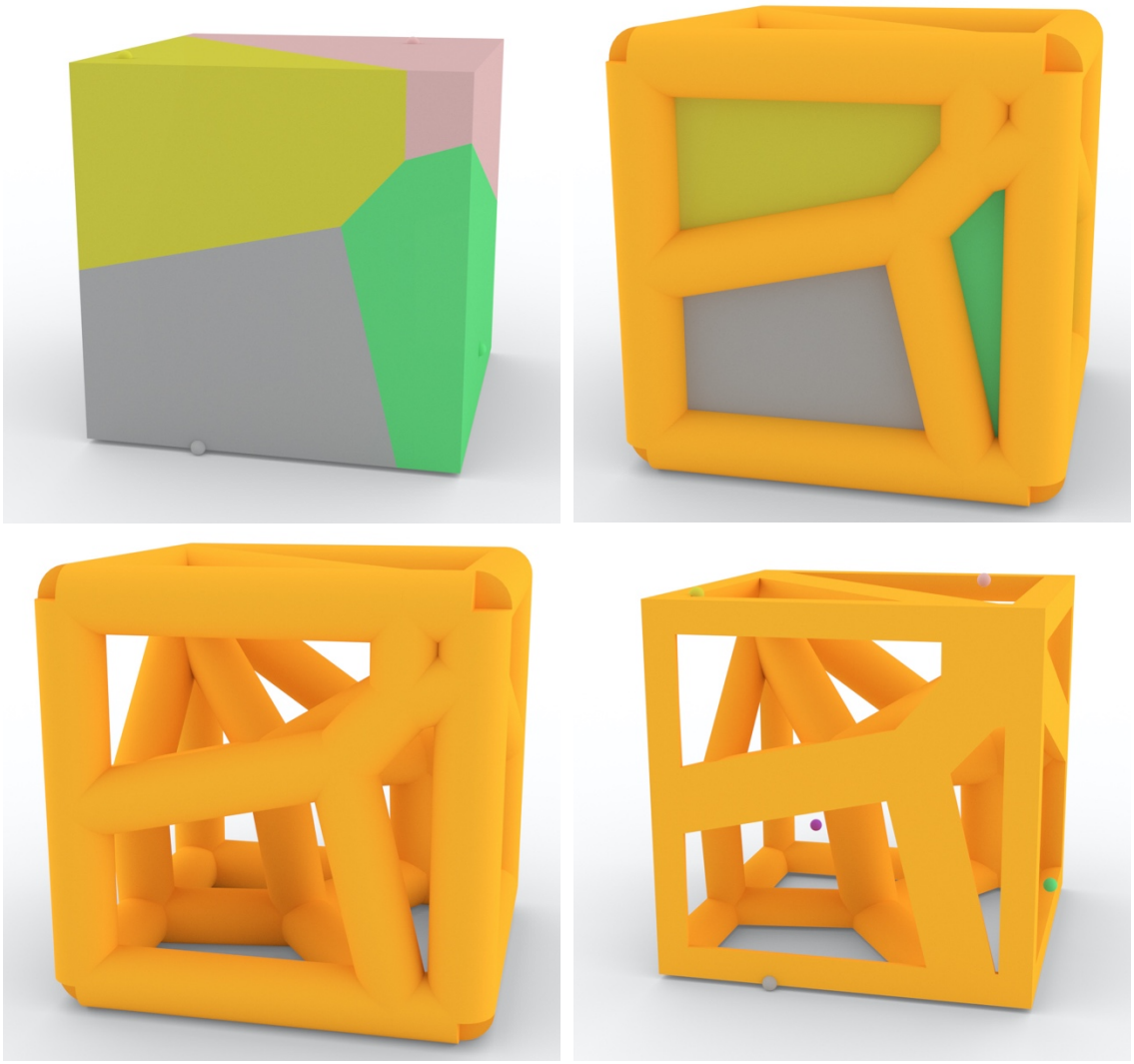

Figure 24 Cylindrical scaffold approach.

Since all the pipe geometries will eventually need to undergo a Boolean Union operation, it was determined that the selected platform performed better with flat ends. Afterwards, the geometry can be clipped to ensure the form is continuous and within the bounds of the original boundary through a Boolean Intersection operation. Referring to Figure 24 again, the original Voronoi tessellation is shown in top-left whereas the top-right figure shows the thickened edges of the Voronoi cells to cylindrical pipes along with the original tessellation. The Boolean Union of the thickened edges is depicted in bottom-left image whereas the original Voronoi sites and the resulting Cylindrical Scaffold can be seen in the bottom-right image.

The second approach is the Extrusion scaffold which is shown in Figure 25. Instead of working with the edges, this approach operates on the cells of the original Voronoi sites seen in top-left image. Each cell is scaled down by a factor φ as illustrated in the top-right corner, and their resulting faces are extruded outwards to the face of the original cell. A Boolean Union operation joins the scaled cells and extrusions into a single form as is noticed in bottom-left image. The Boolean Intersection of this union with the target boundary results in the Extrusion Scaffold as shown in the bottom-right image. This method has been utilized in the literature previously to additively manufacture bone implants by Gomez et al. (2016).

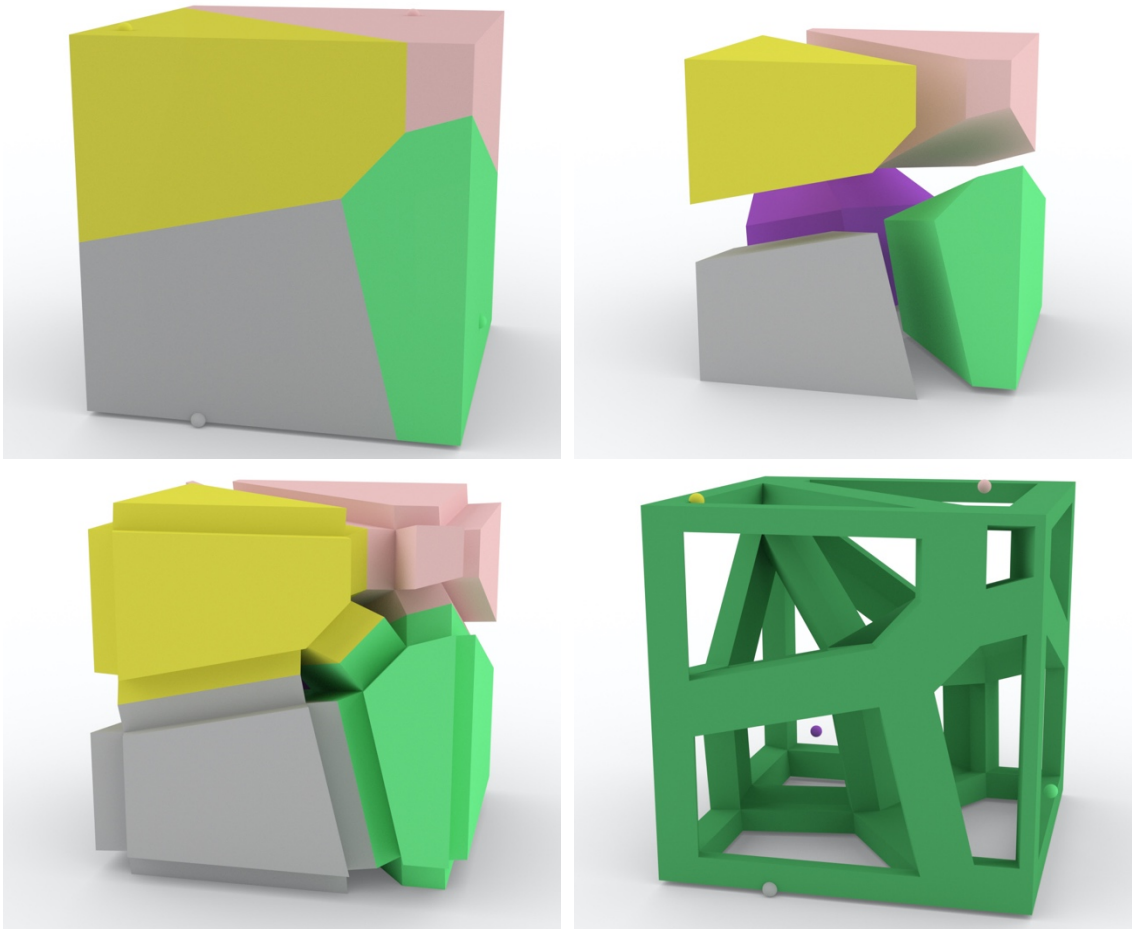

Figure 25 Extrusion scaffold approach.

Third approach is the Procedural scaffold, introduced by Martínez et al. (2016), working primarily with discrete points as shown in Figure 26. The complete design space of the original tessellation, seen in top-left image, is divided into voxels such that each voxel contains a randomly selected single point represented in top-right. The distance of these points is queried from the Voronoi sites, to determine their host cell. Subsequently the distance of these points from their host cell edges is calculated. If the distance is below the threshold τ then the voxel

corresponding to that point is included for the Boolean Union operation shown in the bottom-left image. Their union, seen in the bottom-right, is the eventual Procedural Scaffold of the Voronoi sites.

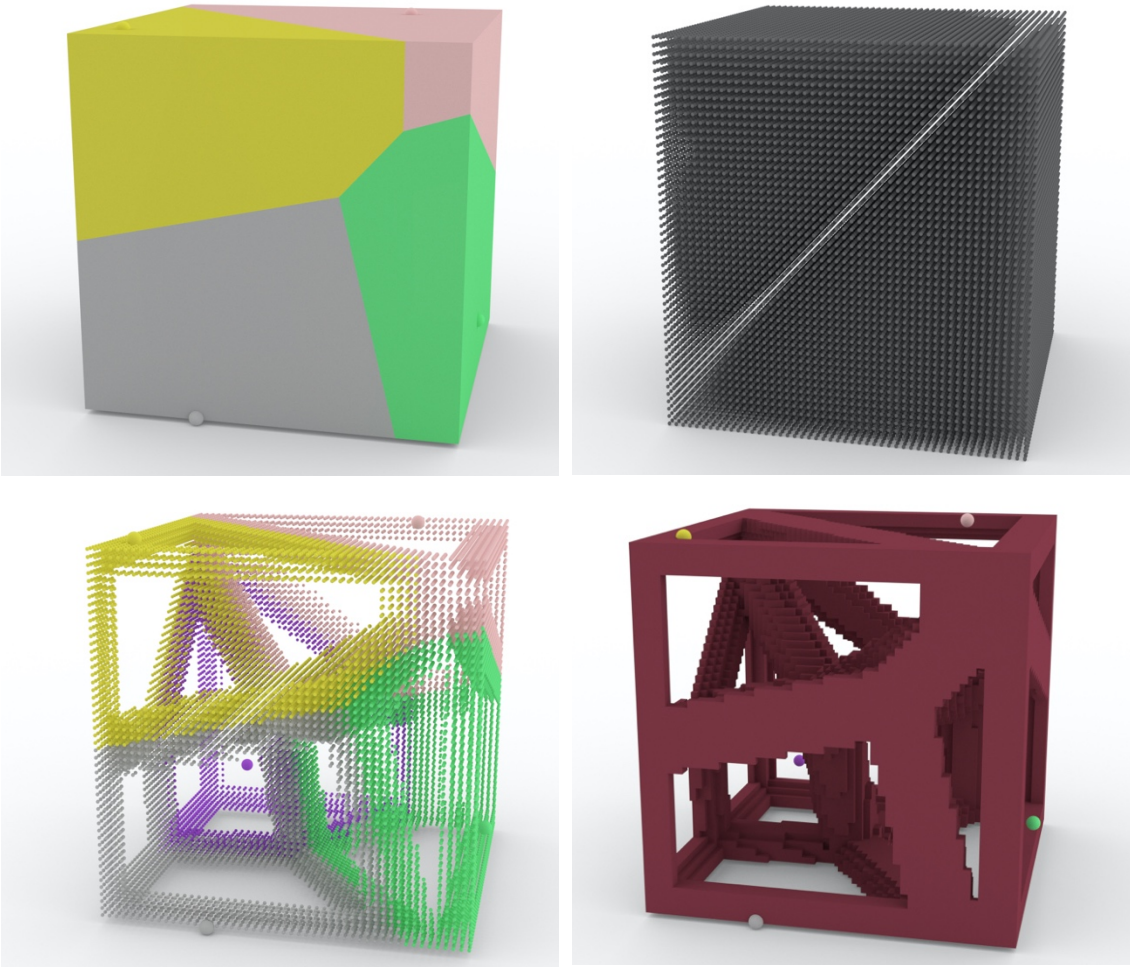

Figure 26 Procedural scaffold approach.

Apart from the three previously mentioned scaffolds, a novel fourth approach is presented in this dissertation. Strategic discretization of edges, faces, and polysurfaces has been harvested to compute this novel Dirichlet-Voronoi

scaffold, or simply referred to as the Dirinoi scaffold to credit both the scholars responsible for presenting the mathematical formulation of the Voronoi tessellation. The outcomes from this approach are displayed in Figure 27.

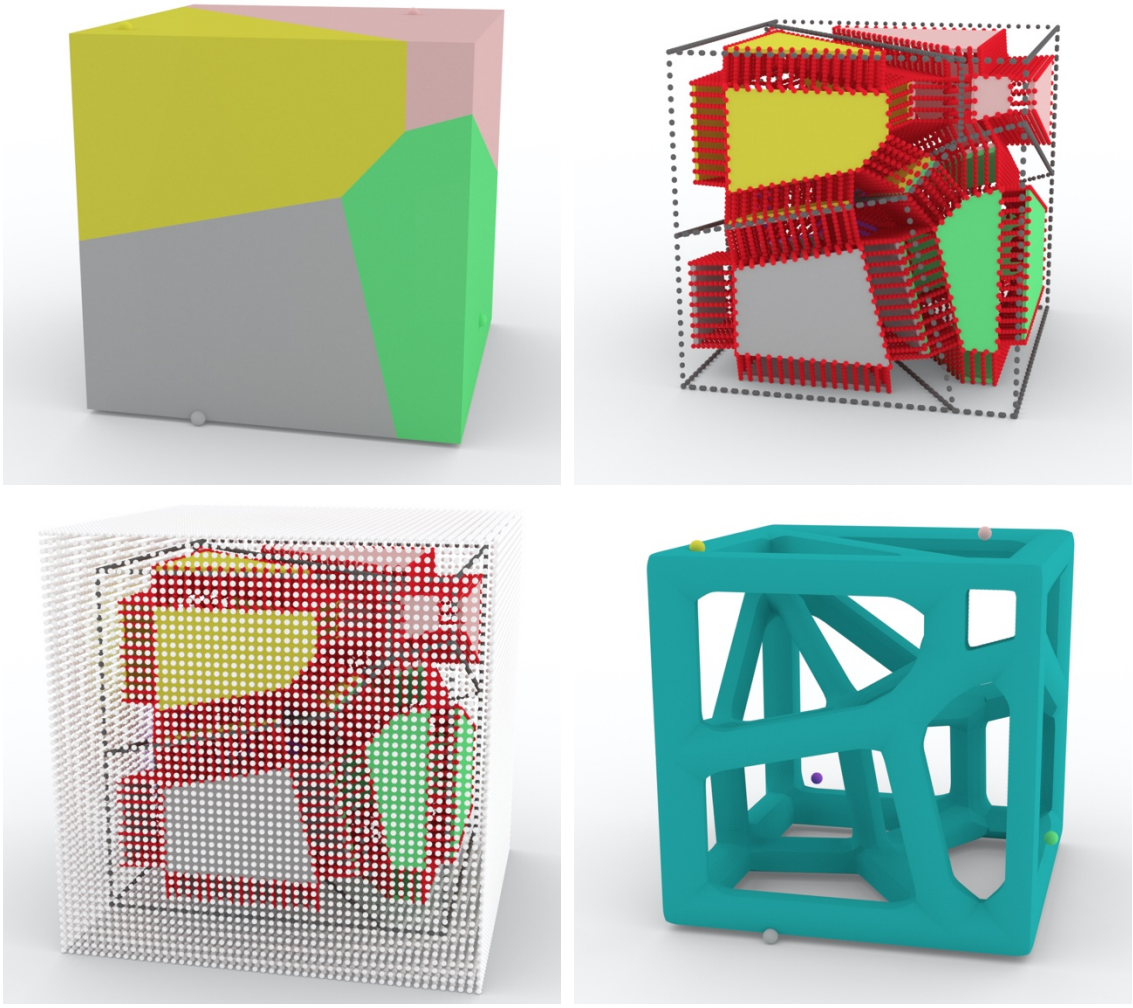

Figure 27 Dirinoi scaffold approach.

Firstly, the edges of the original Voronoi cells, shown in top-left image, are sampled into discrete points separated by a distance λ. These points constitute

the site point collection S_c. In addition, each face of the cell is scaled down by a factor α and subsequently sampled to discrete points, also separated by λ distance. The points obtained from the faces are then offset by a distance ζ along the vector joining the face center and the site of its parent Voronoi cell. The magnitude of these vectors is reduced by multiplication with a scalar δ such that $0 \leq \delta < 1$. This parameter is speculated to be a function of λ and ζ but that determination is outside the scope of this work. The discrete points obtained from sampling the scaled faces and their offsets constitute the neighboring point collection N_c. The sampled site point collection S_c along with the sampled scaled faces and their internal offsets is visible in the top-right image. A new Voronoi tessellation is computed with site point collection S_c as the new sites and neighboring point collection N_c as the neighbors that will bound these tessellations. The result is a collection of Voronoi cells whose Boolean Union represents the Dirinoi scaffold as seen in the bottom-right part of Figure 27.

Additional modifications are recommended to ensure that the Dirinoi scaffold results in convex boundary cells. Firstly, the original Voronoi tessellation is scaled down by a factor Ψ while another geometry is introduced by scaling the original Voronoi tessellation by a factor $\frac{1}{\Psi}$ such that $0 \leq \Psi < 1$. The faces of this scaled up geometry's surface is discretized by distance λ and added to the neighboring point collection N_c as seen in the bottom-left image. Meanwhile, the points that were sampled from the faces, and were offset by a distance ζ along the vector joining the face center and the site of its parent Voronoi cell are offset

by the same distance in the negative vector direction if those faces overlap with the original Voronoi tessellation boundaries. They are also added to the neighboring point collection N_c to finish the modified collection. This ensure that the resulting form is exactly within the boundary of the original cell, and that the Voronoi cells of the Dirinoi scaffold are convex at the boundaries as well.

The Dirinoi scaffold approach involves a hierarchical computation of the Voronoi cells. This hierarchical computation can be continued to further create fractals of porous scaffold, and to be termed as Dirinoi fractals hereon. This concept has striking similarity to the Mandelbrot sets as presented by Mandelbrot (2013). Hence, this approach has the potential to combines two very powerful mathematical concepts, both of which are found abundantly in Nature. Moreover, recent studies such as Molotnikov et al. (2019) have suggested that third and fourth level of hierarchy, in general, are capable of delocalizing strain.

The four aforementioned scaffolds were evaluated for 10 different sets of five (5) Voronoi sites inside a 10x10x10 unit cube. The results are tabulated in Appendix A and have been visualized using a radar graph as shown in Figure 28 to compare the various potential solutions to introduce porosity. The Extrusion scaffold showed significant advantage over the other approaches in three of the five comparison criteria on the shortlisted testing platform. Dirinoi Scaffold had favorable outcomes on the other two criteria. It is to be noted that testing on a different platform, than the one used here, might lead to different results especially for Geometry Union.

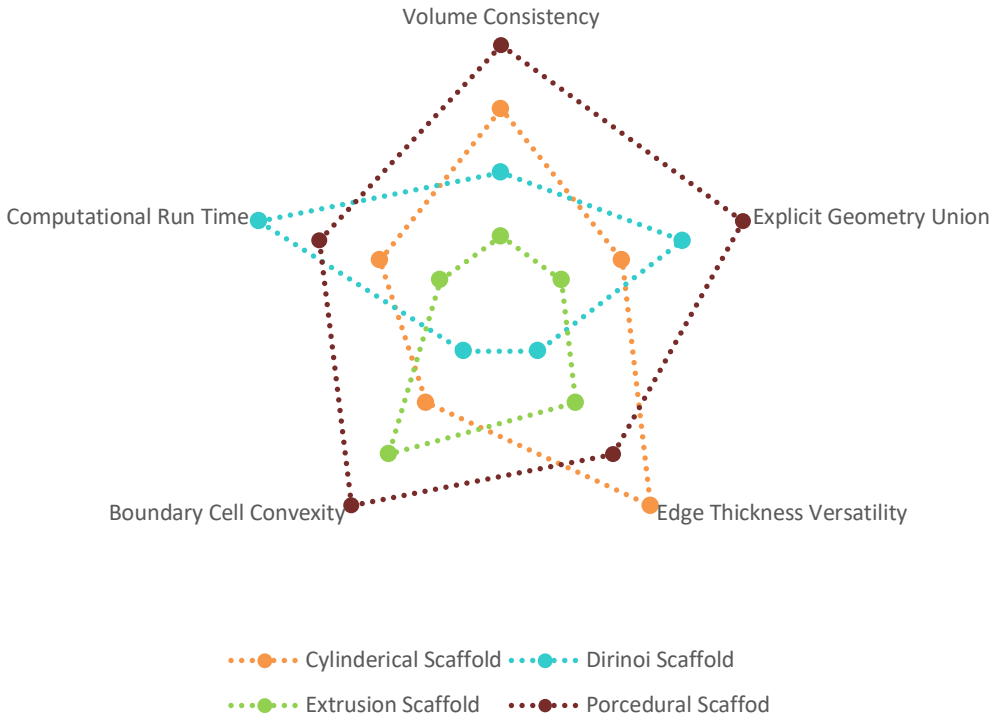

Figure 28 Scaffold evaluation for Voronoi cells boundary representation.

The Volume Consistency evaluates whether the volumetric *Boundary Representation* of the edges remains consistent for all the 10 random sets of dispersing the five Voronoi sites inside the cube. Since the evaluation did not include use of implicit functions, the resulting forms are required to undergo an explicit Boolean operation to union the resulting geometry from either the edges for Cylindrical scaffold and Extrusion scaffold, or the voxels and cells in case of Procedural scaffold and Dirinoi scaffold respectively. The computational expense was also analyzed by measuring the run time for each successful operation. Meanwhile, the Edge Thickness versatility refers to the ability of the scaffold to

account for preservation of the edges that otherwise might be lost during the Boolean Union or due to the inability of the scaffold to wary the thickness relative to their size and position. Lastly, the convexity of the boundary cells is also taken into consideration.

Based on these criteria, the Extrusion scaffold was selected to obtain the *Boundary Representation* of the Voronoi tessellation. Since the same scaffold will be utilized for comparing all the outcomes of this study, its impact on the stress is speculated to be consistent for all the structural simulations. While evaluating the relation between the scaffold approach and mechanical stresses is outside the scope of this investigation, future studies are strongly encouraged to compare the four scaffolds for their impact on the structural performance.

III.2 Stress-weighted Voronoi Tessellation

Upon determination of the ability to create and control porosity of Voronoi tessellation to a satisfactory degree, the critical area of investigation was to determine the technique to parametrically vary the Voronoi sites and the subsequent tessellation for improving the structural performance.

For a fixed count of Voronoi sites, their movement to a new position can be carried out either by replacing the current coordinates with a new set of coordinates or by translating the current coordinates by a specific distance in a specified direction. Since no prior studies exist on any ideal route of movement, only viable possibility is to replace the current set of coordinates with a new set of

coordinates that are determined by the output of the stress analysis from the previous generation. The Lloyd's algorithm is one technique that is often employed to generate new set of Voronoi sites based on the Voronoi cells of the previous generation such that the centroid of the Voronoi cells replaces the Voronoi sites at each iteration. This investigation proposed replacing the sites with a parametrically weighted centroid of the Voronoi cells of the previous generation. By doing so, the new centroid is a function of both the spread of the Voronoi cell as well as the objective parameter, in this case the stresses, as defined by their relative weight.

However, there are many ways to define this weight, and so to limit the scope of this study, the weights can either be directly proportional to the stresses developed in the Voronoi cell or the weights can be inversely proportional to the stresses developed within the Voronoi cell.

In simple term, for directly proportional weights, if the points inside the Voronoi cell have high stress then that point contributes relatively more to the determination of the new stress-weighted centroid. The points that have low stress contribute less to the calculation of the new centroid. Overall, the new Voronoi site, which is the stress-weighted centroid of the previous Voronoi cell, moves towards the region of high stress at each iteration.

Conversely, when the weights are inversely proportional, the points that have high stress contribute relatively less to the determination of the new stress-weighted centroid. The points that have low stress contribute more to the

calculation of the new centroid. Overall, the new Voronoi site, which is the stress-weighted centroid of the previous Voronoi cell, moves towards the region of low stress during each iteration.

This approach of varying the sites to a stress-weighted centroid, thereby creating a parametric Voronoi tessellation for structural optimization, will be referred to as Parametric Insitu Voronoi Optimization Technique (PIVOT) for the rest of this text. The generalized pseudocode for this technique is presented below.

$\forall \{\mathcal{S}_i\}_1^n \subset B$

Compute the Voronoi Cells C_i

Compute the Voronoi Scaffold

Run Finite Element Analysis

$\forall \{\mathcal{S}_i\}_1^n \subset B$

if $\{p_j\}_1^k \subset C_i$

$\bar{i} = \frac{\sum_0^k (p_j * w_j)}{\sum_0^k (w_j)}$

$\bar{i} \rightarrow i$

where B is the optimization bound, C_i is the Voronoi cell corresponding to the Voronoi site $\mathcal{S}_i$, p_j are the coordinates of the j^{th} finite element analysis node (among a total k nodes) and s_{p_j} is the Equivalent (von-Mises) stress at p_j. Here, w_j represents the weight associated with stress-weighted centroid computation. As stated earlier, this weight could be directly proportional to the stresses

developed, which for this investigation was equated such that $w_j = s_{p_j}$ and is referred to as PIVOT Treatment A hereon. The other possibility, where the weight is inversely proportional, was defined such that $w_j = \frac{1}{s_{p_j}}$ and will be referred to PIVOT Treatment B for the rest of this text.

III.3 Research Hypothesis

This study intended to investigate PIVOT, with iterative determination of the new set of Voronoi sites through a stress-weighted centroid computation and subsequent porous carving. The two approaches to compute the weights, as mentioned previously, needed to be tested for their effectiveness. In order to make an informed decision, a benchmark was needed for evaluation. Currently, there exists only one method to iteratively vary the position of the Voronoi sites based on the prior generation sites' position, the Lloyd's algorithm. This is a strictly geometric approach which computes the volume of the Voronoi cell and replaces the Voronoi site with the volumetric centroid of the Voronoi cell at every iteration.

The null hypothesis of the investigation was that there will be no statistically significant difference between the standard deviation of stress from Lloyd's algorithm and the standard deviation of stress from the PIVOT algorithm, from Treatment A as well as Treatment B. The alternative hypothesis is that there will be statistically significant difference between the standard deviation of stress from Lloyd's algorithm and the standard deviation of stress from PIVOT algorithm, Treatment A and Treatment B.

III.4 Research Objective

The research objective was to answer the research question by developing a methodology to test the research hypothesis of this investigation on 3D full MBB beam. A successful rejection of the null hypothesis establishes that the proposed technique, a stress-weighted centroid, is significantly distinct from the Lloyd's algorithm, which is the geometric centroid, for structural optimization purposes. A failure to reject the null hypothesis means further studies are required before making an informed decision.

CHAPTER IV

METHODOLOGY

The PIVOT algorithm proposed in this dissertation was tested using computational simulations. More specifically, the test was setup to determine changes in the internal form without any disturbance in the external profile and boundaries for the purposes of this study.

A standalone workstation, Intel® Core™ i7-7700K CPU @ 4.20GHz, 64 GB RAM with GeForce GTX 1080 NVIDIA GPU, was used with Ada, an Intel x86-64 Linux cluster on the Texas A&M University High Performance Research Computing (HPRC) platform.

IV.1 Research Approach

The geometry was generated in *Rhinoceros 7* software by McNeel (2015) and the supporting graphical programming interface *Grasshopper3D* by Rutten (2015). This geometry was later exported to the *ANSYS Workbench 2019 R3 Academic*, as detailed by Kohnke (1982), to conduct the static structural simulations. The results noting the stress distributions were looped back into the *Rhinoceros 7* platform for determining the geometry for the next iteration. At this stage of the investigation, the process was carried out manually, but it can be automated later on. The outline of the data cycle is displayed in Figure 29.

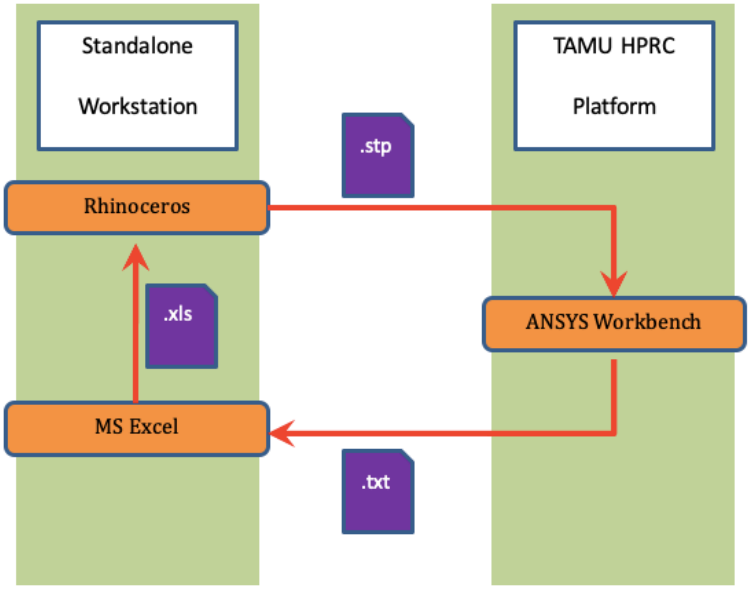

Figure 29 Schematic of the information flow.

The computation of the stress-weighted centroid to successively replace the Voronoi site of the previous iteration was computed in *Rhinoceros 7-Grasshopper3D* interface for PIVOT Treatment A and PIVOT Treatment B. Since the Lloyd's algorithm does not need any input from the stress analysis, all the iterations were generated in the *Rhinoceros 7-Grasshopper3D* interface directly. However, all the resulting forms were then exported to *ANSYS Workbench* to analyze and compare their structural performances.

IV.2 Preliminary 2.5D Study

The algorithm was tested on a 2.5D full MBB beam specimen in a preliminary study. The material assignment was structural steel for all static structural analysis purposes. The density of the material was set to 7850 kg/m^3,

the Young's Modulus was 200 GPa. This material had a Tensile Yield Strength of 250 MPa, and the Tensile Ultimate Strength of 460 MPa. The element size for finite structural analysis purposes was set to 0.5 mm.

The loading conditions and the boundary conditions were equivalent to a simply supported beam. The length of the beam was 6L, the height was L, and the thickness was 0.1L while the support and loading block dimensions were ΔL x 0.1L x 0.1L. For this investigation, L was fixed to 10mm and ΔL was set to 2mm. A load of 100 N was acting on the top of the beam. The Extrusion scaffold factor was fixed ($\varphi = 0.755$) such that the volume of the porous scaffold was 15 percent of the total volume of the boundary to be optimized, thereby achieving 85 percent porosity. Fixing the porosity ensures that the overall volume of material is not changed but only repositioned based on the changes in the Voronoi sites.

A 2D Voronoi tessellations was generated for the initial beam with 50 randomly selected sites. Subsequently, 20 iteration of the control and 20 iterations for each of the two treatments were carried out to analyze the changes in the structural performance. The 2.5D geometry resulting from the extrusion of 2D Voronoi Tessellation was computationally evaluated for the mean stress, maximum stress, and the standard deviation of stress in addition to collecting the total strain energy for each beam.

The starting distribution of the 50 Voronoi sites is shown in the top image of Figure 30. The red highlight represents the collection of Voronoi sites whose cell edges form the boundary of the full MBB beam. It is noteworthy that some of

the sites are closer to the boundary while others are relatively away from the beam outline. The image on the bottom displays the Equivalent (von-Mises) stress developed in the beam that were obtained by this distribution of Voronoi sites. The outer boundary is noticeably thinner than the inner members because the inner members were union of adjacent cell while the external ends of the beam were resulting from a single cell. The white outline shown in the bottom image was also separately analyzed to exclude the impact of thin boundary members.

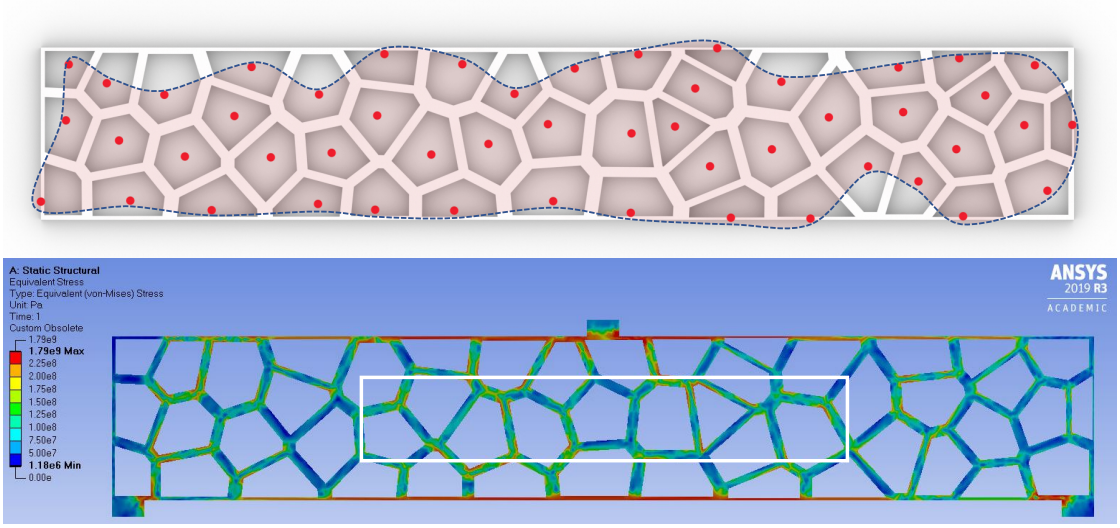

Figure 30 Initial beam at zero (0) iteration with 50 Voronoi sites.

The Voronoi sites shown in Figure 30 underwent the Lloyd's algorithm for 20 iterations. The resulting distribution of Voronoi sites, and the corresponding structural performance for the same boundary and loading conditions as the initial beam, is depicted in Figure 31. The Voronoi sites were more uniformly distributed, and the collection of Voronoi sites whose cell edges form the boundary of the MBB

beam appear at a comparatively consistent distance from the edge regardless of the stresses developed in the regions as displayed in the bottom image.

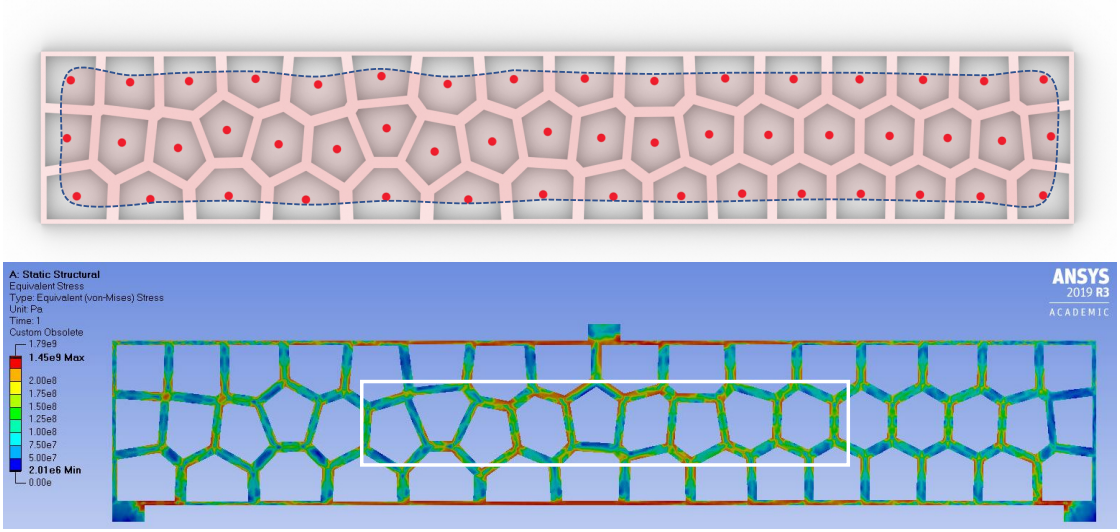

Figure 31 Form and performance of the beam after 20 iterations of Control.

The definition of PIVOT Treatment A termed the weights directly proportional to the stresses developed at the nodes inside the Voronoi cells. Since the top and bottom edges have higher stresses, the Voronoi sites appear to be near those edges, after 20 iterations, as seen in the top image of Figure 32. As compared to the initial beam in Figure 30 and the control beam in Figure 31, the collection of Voronoi sites is very close to the edges especially in the middle third section that had high stresses as evident from the stress contours in the bottom image. Since the stresses are higher across the center third of the top and bottom band, it could be restricting the Voronoi sites from concentrating closer together.

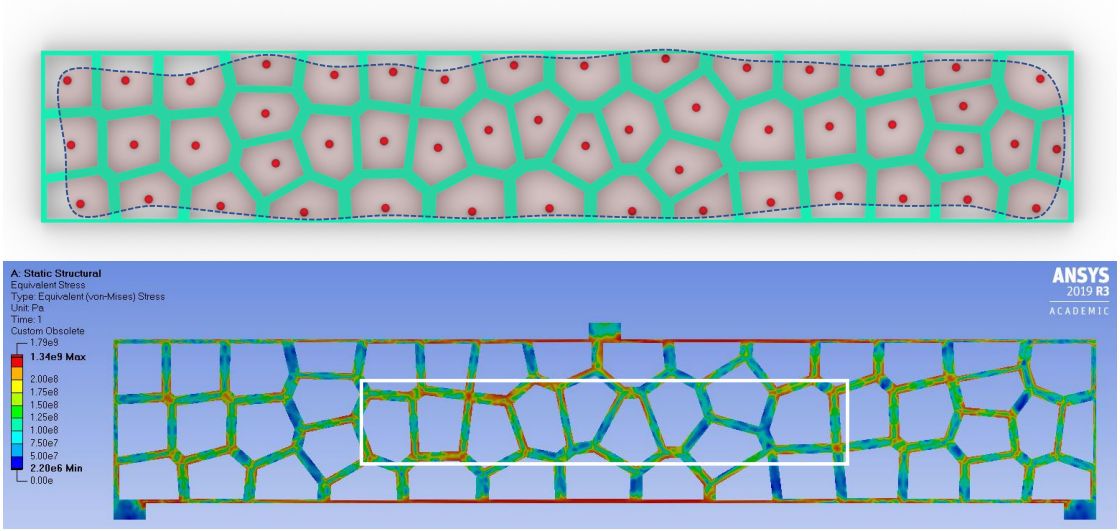

Figure 32 Form and performance of the beam after 20 iterations of PIVOT Treatment A.

On the other hand, PIVOT Treatment B defined the weights inversely proportional to the stresses developed at the nodes inside the Voronoi cells. Since the top and bottom edges have higher stresses, at the end of 20 iterations, the Voronoi sites appear to have concentrated away those edges as seen in the top image of Figure 33. This was significantly different from the previous observations.

Additionally, the Voronoi sites appear to have concentrated in top left and top right regions which also display lower stresses compared to the rest of the space. The resulting structural performance was also comparatively different than the previous techniques as there is a reduction in the Equivalent (von-Mises) stress especially in the middle regions denoted by the white outline. Across 20 iterations of the three techniques, PIVOT Treatment B outperformed the other two techniques across the measured parameters.

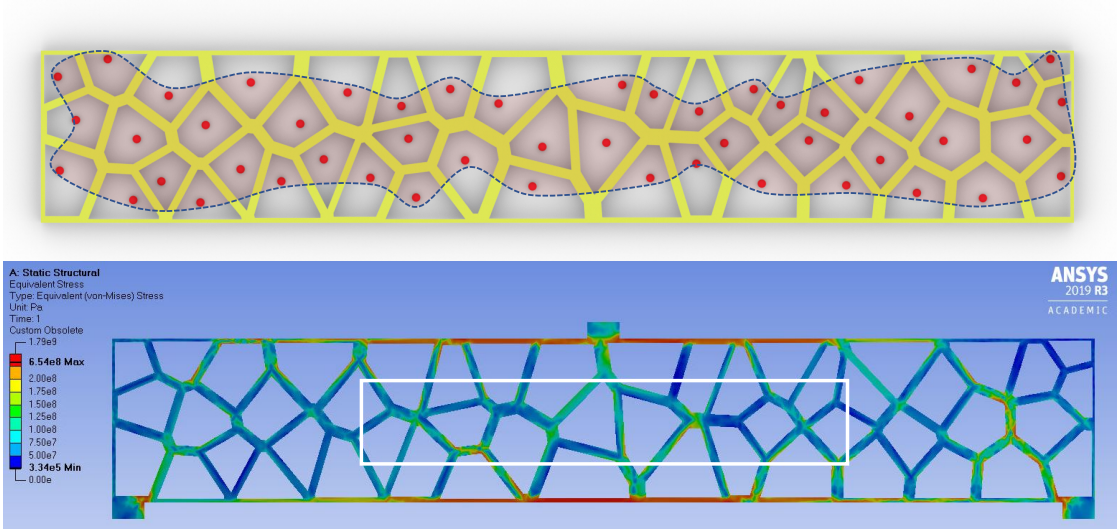

Figure 33 Form and performance of the beam after 20 iterations of PIVOT Treatment B.

The summary of comparison between the initial iterations and the change observed at the end of 20 iterations is presented in Table 1.

Table 1 Summary of nodal stress data for 2.5D study after 20 iterations.

	Standard Deviation of Stress	Mean Stress	Maximum Stress
Lloyd's Algorithm	93.0%	108.2%	80.7%
PIVOT Treatment A	106.3%	125.2%	74.7%
PIVOT Treatment B	75.0%	72.5%	36.5%

Additionally, the standard deviation of stress and the mean stress was also plotted against every iteration and is depicted in Figure 34. A majority of change, across the three techniques, was observed in the first 10 iteration with minor adjustments in the next 10 iteration as evident from the same figure.

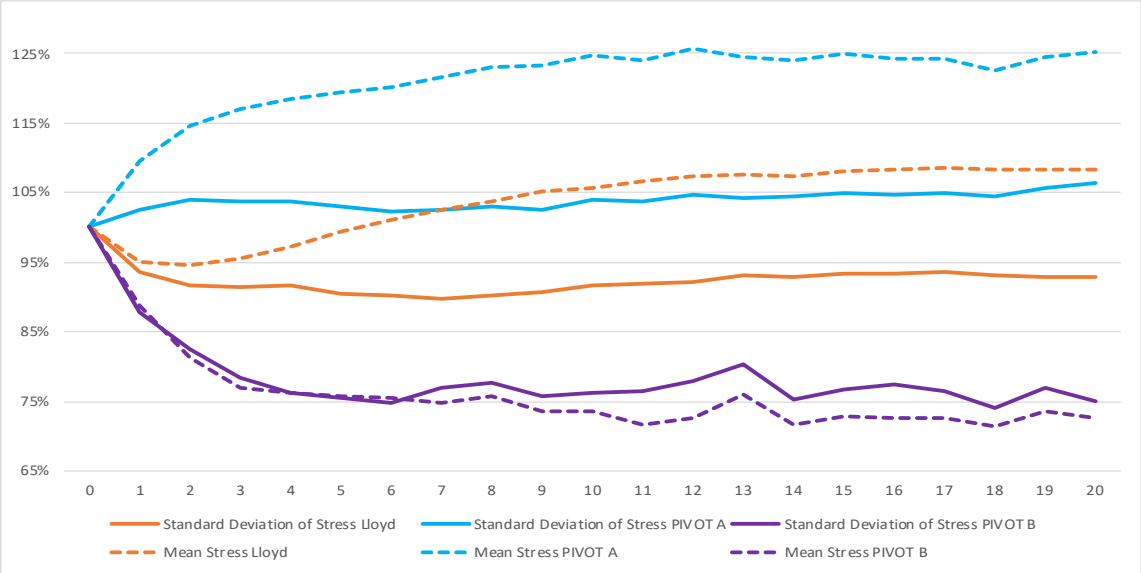

Figure 34 Changes in standard deviation of stress and mean stress in 2.5D beam across 20 iterations.

For the standard deviation of stress, the Lloyd's algorithm noticed an 8.3% reduction in first 10 iterations and a 1.3% increase in the next 10 iteration. PIVOT Treatment A showed an increase of 4.0% followed by another increase of 2.3% percent while PIVOT Treatment B showed a 23.8% decrease followed by another 1.1% decrease in the first and next 10 iterations respectively.

Similar trend was observed for the mean stress. The Lloyd's algorithm resulted in a 5.7% increase during the first 10 iterations and another 2.5% increase during the next 10 iterations. PIVOT Treatment A was responsible for a 24.7% increase in the first 10 iteration and an additional 0.4% net difference was observed between the 10^{th} and the 20^{th} iterations. PIVOT Treatment B resulted in 26.5% reduction during the first 10 iteration and another 0.9% reduction during the next 10 iterations.

As stated earlier, the structural performance of the inner sections of the beams was also analyzed separately to control for the impact of the thinner boundary members. The results are visualized in Figure 35, and PIVOT Treatment B continued be the most favorable technique. The inner members that were analyzed have been depicted with a white outline in the bottom images of Figures 31, 32 and 33.

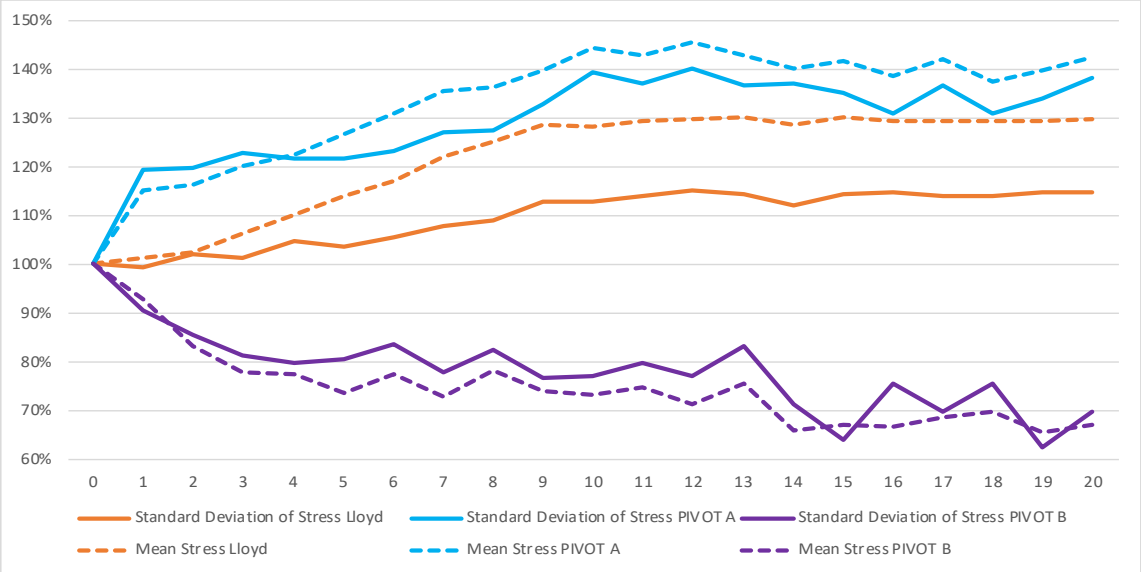

Figure 35 Changes in standard deviation of stress and mean stress in 2.5D beam across 20 iterations for the inner members.

Additionally, the total strain energy of the beam was recorded and plotted against the iterations in Figure 36. The Y-axis denotes the energy in milliJoules (mJ) while the X-axis represent the iteration number. Over 20 iterations, the Lloyd algorithm resulted in a net increase of 12.8% while PIVOT Treatment A displayed a net increase of 38.8%. PIVOT Treatment B was the only technique to show a

reduction, with 34.0% lower total strain energy as compared to the initial starting beam. Again, a majority of the change was observed in the first 10 iterations as compared to the next 10 iterations. The Lloyd's algorithm and PIVOT Treatment A had net increases of 9.1% and 36.9%, respectively, in the first 10 iterations while PIVOT Treatment B had a net decrease of 33.5% in the first 10 iterations. The rest of the net change was recorded in the next 10 iterations of the respective techniques. The structural performance parameters collected for the 2.5D beam are provided in Appendix B.

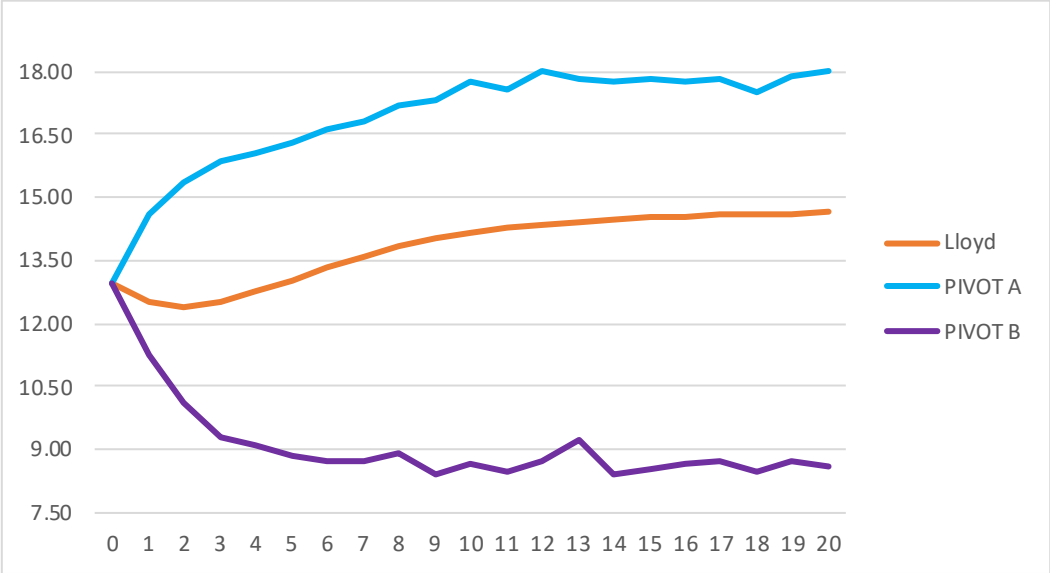

Figure 36 Total strain energy for the 2.5D beam.

IV.3 Research Design – 3D Specimen

The research objective of this investigation was to test the hypothesis on a typical 3D full MBB beam specimen as obtained by computation of Voronoi

tessellation in 3D space. The rest of this text refers to the 3D study. The material assignment was structural steel for all static structural analysis purposes. The density of the material was set to 7850 kg/m^3, the Young's Modulus was 200 GPa, and this material was recorded to have a Tensile Yield Strength of 250 MPa, and the Tensile Ultimate Strength of 460 MPa. The element size for finite structural analysis purposes was set to 1mm.

The loading conditions and the boundary conditions were equivalent to a simply supported beam as displayed in the Figure 37. In accordance with the typical full MBB beam requirements, the length of the beam was 6L, the breadth and height were L. The support and loading block dimensions were ΔL x L x 0.1L. For this investigation, L was fixed to 10mm and ΔL was set to 2mm. A 100 N force was acting on the top of the loading block.

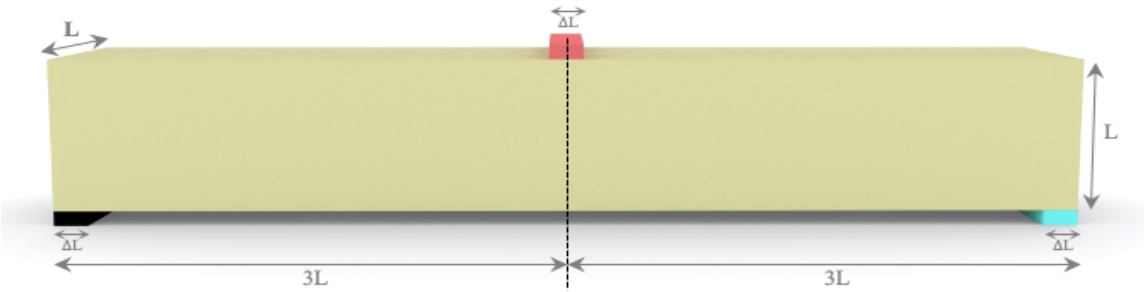

Figure 37 Full MBB beam test specimen.

Referring to Figure 37, the bottom face of the left support block was assigned as a fixed surface with no allowable displacements, that is, no translations or rotations. The bottom face of the right support block was assigned

as a frictionless surface where it was allowed to move in the horizontal direction but translations in other two dimensions were restricted, and only one rotation was allowed while restricting the other two.

The Extrusion scaffold factor was fixed ($\varphi = 0.755$) such that the volume of the porous scaffold was 15 percent of the total volume of the boundary to be optimized, thereby achieving 85 percent porosity. Fixing the porosity ensured that the overall volume of material is not changed but only repositioned based on the changes in the Voronoi sites.

The objective of this investigation was to test the null hypothesis on a 3D full MBB beam, such that there will be no significant difference between the standard deviation of stress from the Lloyd's algorithm and the results obtained from the standard deviation of stress from PIVOT treatments. The alternative hypothesis stated that the difference between the standard deviation of stress from the Lloyd's algorithm and the results obtained from the standard deviation of stress from PIVOT treatments is non-zero and significant.

Since the iteration process was carried out manually, nine (9) iterations were determined reasonable enough to gather insights to determine if the techniques were performing as aspired. However, since only limited iterations were carried out, the initial Voronoi sites can have major impact on the resulting tessellations, as determined from the Lloyd's algorithm and the PIVOT treatments. Therefore, having multiple limited trials ensured a more stable and independent outcome. Additionally, the pure computational nature of this investigation meant

that there were not any external human factors impacting the outcomes and the only reason to review multiple cases was to compensate for the limited number of iterations. Therefore, it was determined that three (3) Cases should be enough to observe whether the techniques display a consistent direction of change in the standard deviation of stress.

Three (3) Cases (I, II, and III) of this investigation contained 25 randomly selected Voronoi sites in each case. From the initial base structure, nine (9) iterations were carried out for the control, that is, the Lloyd's algorithm and nine (9) each for the treatments, PIVOT Treatment A and PIVOT Treatment B.

For instance, in Case I, after randomly selecting 25 Voronoi sites, the initial computation (Iteration 0) of the Voronoi tessellation was carried out and the subsequent porous Extrusion scaffold was determined in *Rhinoceros 7-Grasshopper3D* interface. The geometry was be exported to *ANSYS Workbench* where stresses were determined for the previously stated boundary and loading conditions. After the static structural analysis of Iteration 0, stress-weighted centroids were calculated for each cell and the Voronoi sites were accordingly shifted to their new position within the design space. This constituted the Iteration 1 of PIVOT Treatment A, where weights were directly proportional to the stresses developed inside the cells, for Case I. Upon selection of new Voronoi sites, a corresponding porous Extrusion scaffold was computed before exporting the resulting geometry for the static structural analysis and determining new weights to update the Voronoi site positions for Iteration 2.

Such loop was continued for nine (9) iterations and, similarly, nine (9) beams were analyzed for PIVOT Treatment B. In addition, nine (9) beams, based on the Lloyd's algorithm, were also evaluated for their structural performance. However, as mentioned earlier, the Lloyd's algorithm site determination is independent of the structural results. This process was carried out for Case II and Case III as well with the only difference being the distribution of the 25 initial Voronoi sites constituting the Iteration 0 for each case.

Every unique distribution of the collection of 25 Voronoi sites corresponds to different material placement, which in turn represents a unique beam. These beams can then be grouped according to the technique that was utilized to generate the Voronoi sites. Conducting a t-test evaluation of these groups gives the insights and the ability to determine if any difference exists between the structural performance of these groups. In simpler terms, determining whether the unique distributions of Voronoi sites, as obtained by different techniques, culminate in any difference in their structural performance or are these techniques equivalent to random selections.

Since there are three (3) initial base beams from each case and nine (9) iterations for each of those cases (I, II and III), it results in 27 unique sets of Voronoi sites provided by each technique. The standard deviation of stress was calculated for each beam and added to their respective technique group. Group A (μ_A , σ_{A}, n_{A}), was such that μ_A represented the mean of the standard deviation of stress of beams obtained through the Voronoi sites of PIVOT Treatment A, σ_{A}

is the standard deviation of the standard deviation of stress, and n_{A} is the population of Group A, which was 27. Similarly, Group B (μ_B , $\sigma_{\mathrm{B}}, n_{\mathrm{B}}$) and Group C ($\mu_C$, $\sigma_{\mathrm{C}}, n_{\mathrm{C}}$) corresponded to PIVOT Treatment B and the control – Lloyd's algorithm respectively. A significance level of 0.05 corresponding to a 95 percent confidence interval was adopted for the t-test. The z-value of 1.96 was noted given a two tailed test for a 95 percent confidence interval. The standard error was determined from the following equation where T refers to either Treatment A or Treatment B.

$$SE = \sqrt{\frac{\sigma_{\mathrm{C}}^2}{n_{\mathrm{C}}} + \frac{\sigma_{\mathrm{T}}^2}{n_{\mathrm{T}}}}$$

Based on the standard error the following bound was created to check whether the alternative hypothesis, $\mathrm{N_A}: \bar{\mu}_{\mathrm{C}} - \bar{\mu}_{\mathrm{T}} \neq 0$, was satisfied. Such bound was created for both PIVOT Treatment A and PIVOT Treatment B separately to make determinations whether one of both of them were significantly different from the control, that is the Lloyd's algorithm.

$$(\mu_C - \mu_T) - z_{\frac{\alpha}{2}}.SE \leq \bar{\mu}_{\mathrm{C}} - \bar{\mu}_{\mathrm{T}} \leq (\mu_C - \mu_T) + z_{\frac{\alpha}{2}}.SE$$

CHAPTER V

RESULTS

This chapter presents the results of the computational structural simulations for the 3D full MBB beam study. The investigation was primarily concerned with reducing the stress concentrations in structural form by lowering the standard deviation of stress. Other parameters, such as the mean stress and maximum stress, and the impact of changing the position of Voronoi sites on those parameters is also noted here.

V.1 Data Collection

The primary data collected for this study was the position of the Voronoi sites, which was the independent (input) variable, and the resulting Equivalent (von-Mises) stress, which was the dependent variable. This data has been visually presented here for each of the three (3) cases.

The Voronoi sites have been presented through renderings developed in the *Rhinoceros 7-Grasshopper3D* interface. For visualization convenience, the Voronoi sites have been turned into spheres whose radius was set to 0.25 mm. Meanwhile, the nodal stresses have been presented here with the help of the iso-contours of stress as determined from the static structural analysis in the *ANSYS Workbench* interface. The distribution of Voronoi sites for Case I is depicted in Figure 38 with the initial position of sites in black and the final positions in red.

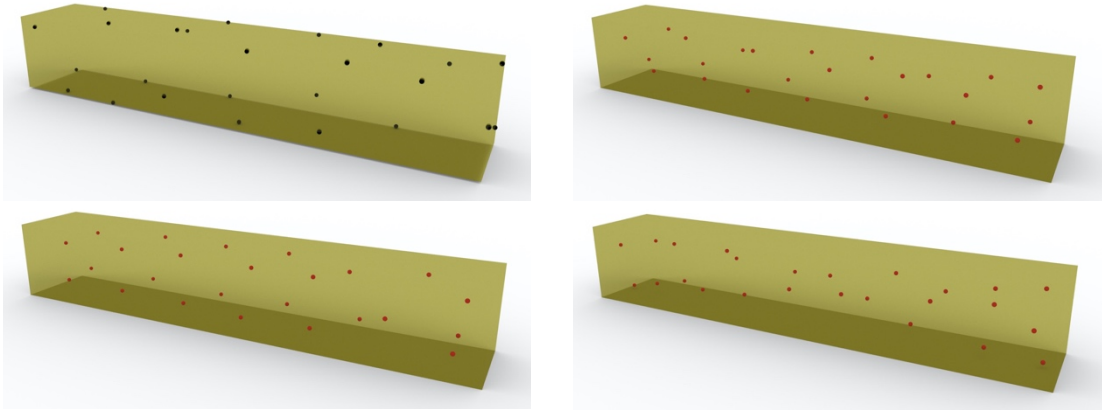

Figure 38 Distribution of Voronoi sites for Case I.

The top left image shows the starting Voronoi site while the top right shows the sites after nine (9) iterations of the Lloyd's algorithm. The bottom left image is the output of ninth iteration of PIVOT Treatment A while Treatment B output is visible in bottom right. Similarly, the distribution for Case II is shown in Figure 39.

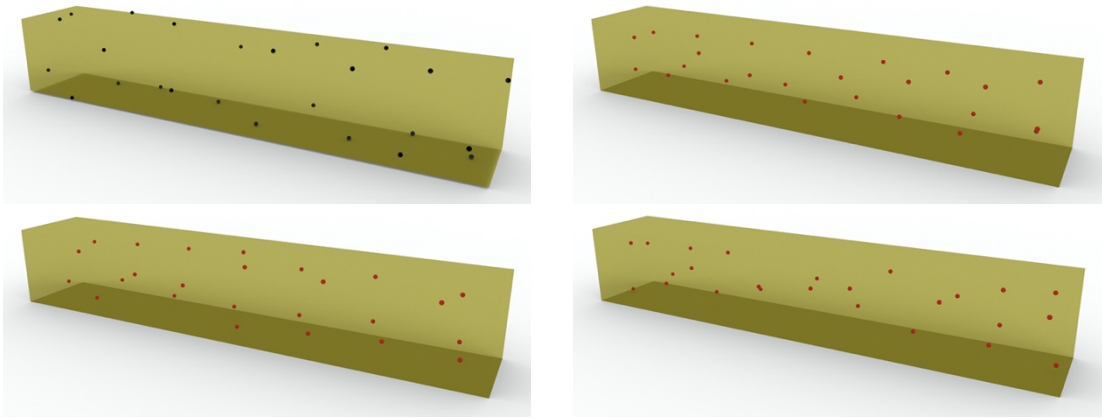

Figure 39 Distribution of Voronoi site for Case II.

Figure 40 depicts the initial Voronoi sites, shown in black, and the final site positions, shown in red, for Case III in a similar template.

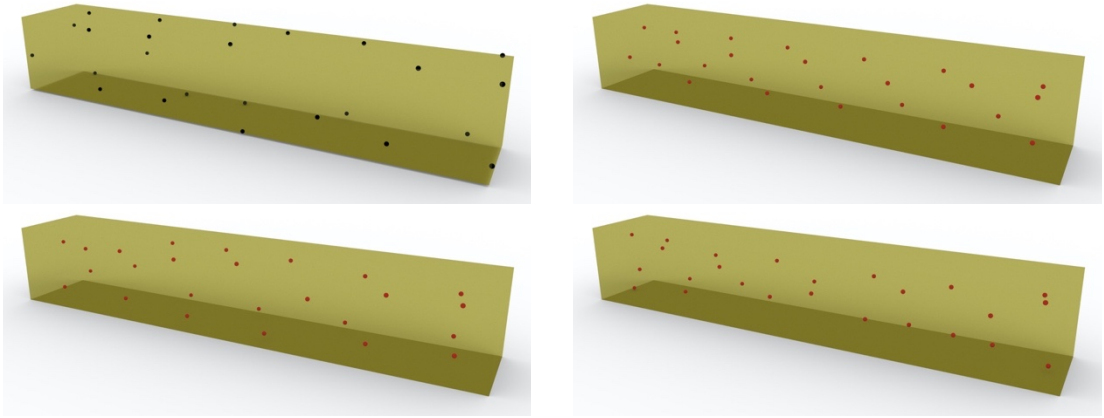

Figure 40 Distribution of Voronoi sites for Case III.

The initial position of Voronoi sites was randomly distributed for all the three (3) Cases. Over course of the nine (9) iterations, the Lloyd's algorithm can be seen supplementing an even distribution of the sites. Meanwhile, PIVOT Treatment A showed a noticeable placement of the Voronoi sites near the extreme ends of the vertical middle section of the beam below the loading strip. On the contrary, PIVOT Treatment B had minimal Voronoi sites in the middle third region.

The collection of structural simulation results also provided some insights regarding the behavior of the porous beam members that correspond to these Voronoi site placements. The tensile yield strength of the material, structural steel, is 250 MPa or 2.500e8 Pa. The stress color legend remains constant in all the structural results with the exception of the top end which is set to the maximum stress of that particular analysis. The output of Case I is shown in Figure 41. As evident from this figure, there is a stress concentration that occurs on the ends near the loading strip which is visible as red patches.

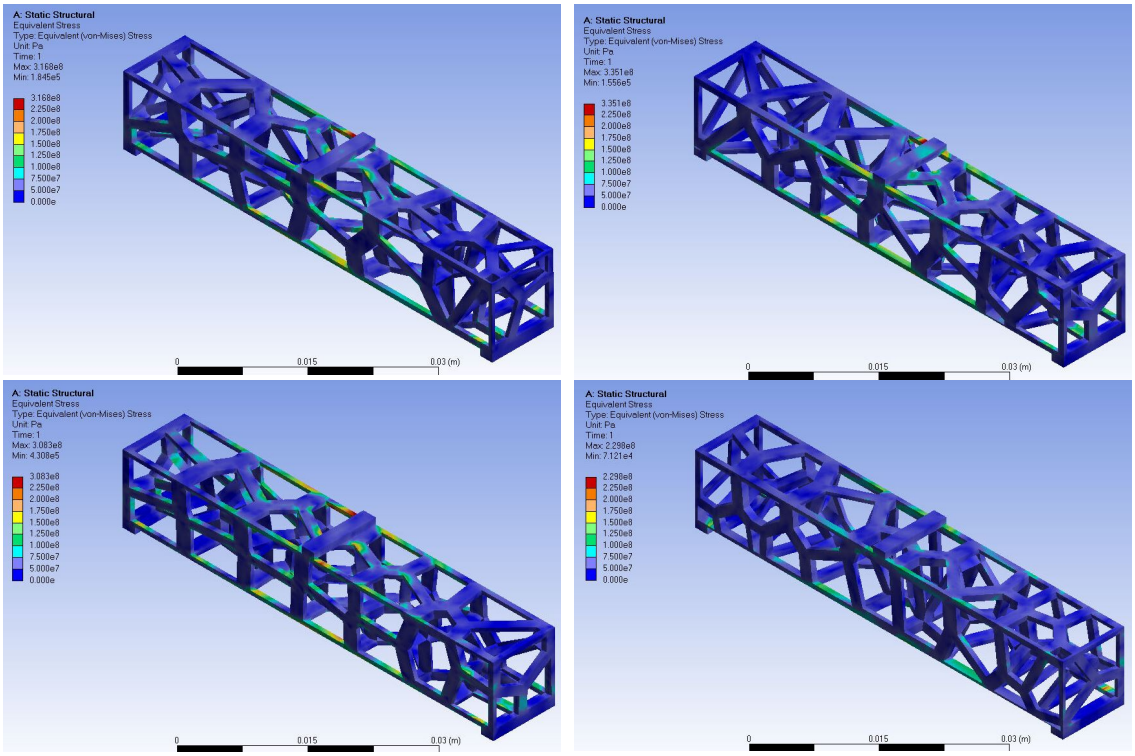

Figure 41 Static structural analysis results for Case I.

The initial structure, shown in top left image is noted displaying this issue. This continues to be the situation for the structural analysis of the end output from the Lloyd's algorithm in the top right image. The member corresponding to the Voronoi sites after nine (9) iterations of PIVOT Treatment A, seen in bottom left, seems to have introduced some additional areas of stress concentration. Meanwhile in the bottom right, the result from PIVOT Treatment B show a reduction in stress concentrations and a removal of the red patch near the loading strip. Case II also illustrated a similar narrative as evident from the Figure 42. It is to be noted that not all stress concentration is visible in the perspective view and might be hindered by the loading strip on top or the internal members themselves.

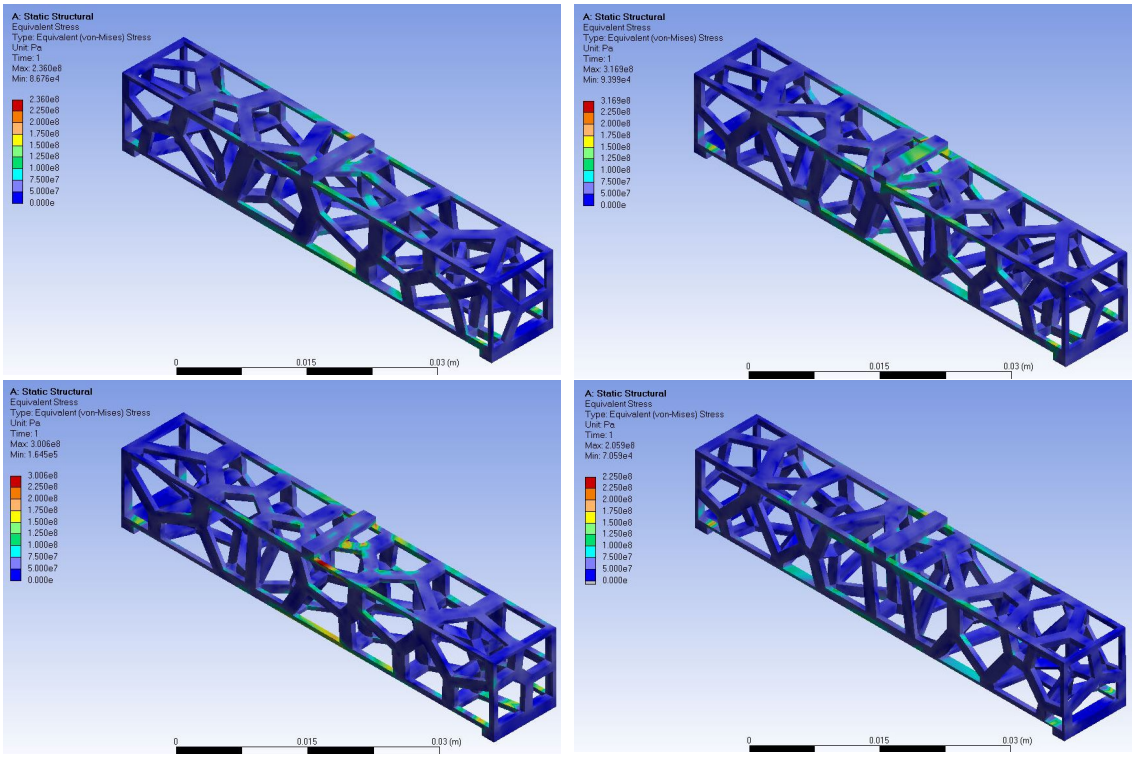

Figure 42 Static structural analysis results for Case II.

Over the nine (9) iterations, the maximum stress significantly increased for the output for the Lloyd's algorithm. PIVOT Treatment A on the bottom left also displayed an increase in maximum stress with the introduction of newer red patch of high stress that were absent in the initial beam. The image of the beam member corresponding to PIVOT Treatment B in bottom right shows an elimination of stress concentration.

The visual representations from Case III, depicted in Figure 43, can be seen paralleling the output of the previous two cases. The initial beam member in top left, the final output from Lloyd's algorithm after nine (9) iterations in the top right, and the final output from PIVOT Treatment A after nine (9) iterations in

bottom left showed stress concentration near the loading strip. This is absent from the output of the ninth iteration of PIVOT Treatment B in the bottom right.

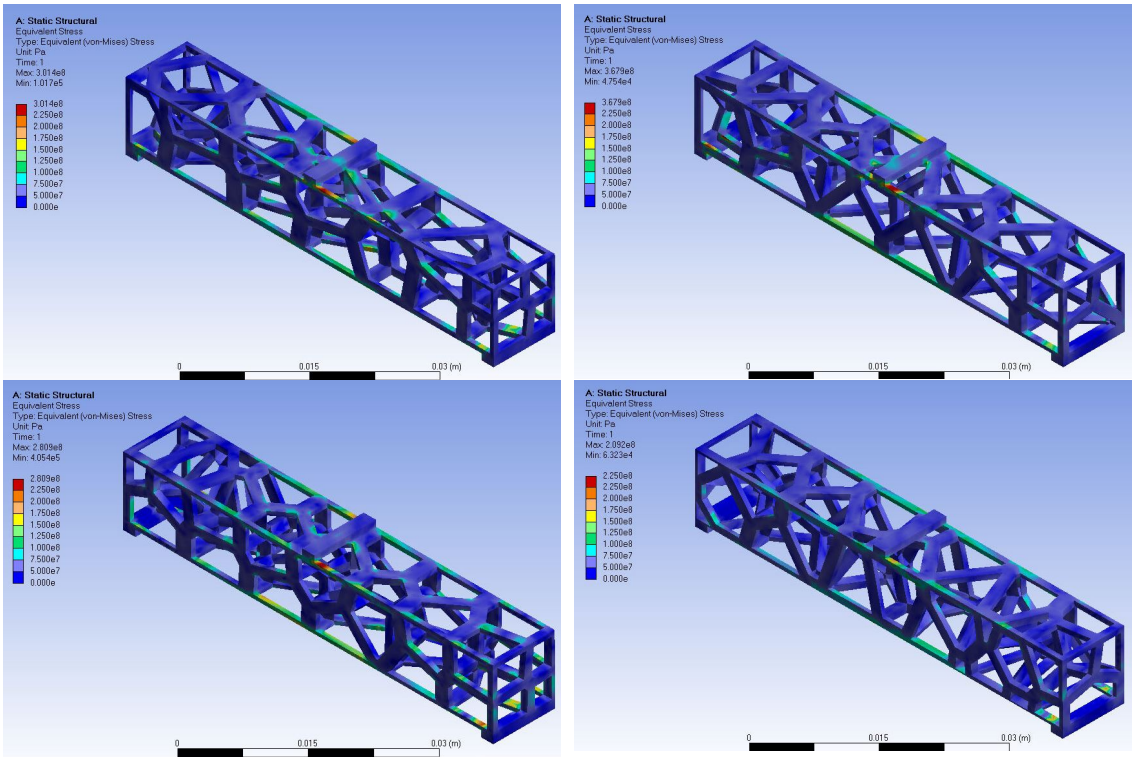

Figure 43 Static structural analysis results for Case III.

V.2 Data Analysis

The Equivalent (von-Mises) stress values collected from the static structural analysis were analyzed for their standard deviations. These stress values were collected at all the nodes corresponding to the mesh element size of 1mm. A majority of the times, the total number of nodes, across the initial beam, control beams and the treatment beams, were between 27,000 and 29,000. Each Case contained a total of 28 beams – one (1) initial base beam, nine (9) control

beams from the Lloyd's algorithm, and 18 treatment beams with nine (9) beams from PIVOT Treatment A and nine (9) beams from PIVOT Treatment B.

Across the 28 beams in Case I, a maximum of 28,888 nodal stresses and a minimum of 27,522 nodal stress were available for analysis. The results, at the end of nine (9) iterations, from Case I are presented in Table 2. The initial base beam results, with standard deviation of stress of 28.82 MPa, mean stress of 30.03 MPa, and a maximum stress of 316.84 MPa, were the 100 percent standards. This was compared with the ninth iteration of the three (3) techniques.

Table 2 Summary of nodal stress data after nine (9) iterations for Case I.

	Standard Deviation of Stress	Mean Stress	Maximum Stress
Lloyd's Algorithm	101.4%	97.3%	105.8%
PIVOT Treatment A	111.3%	119.5%	97.3%
PIVOT Treatment B	79.9%	89.7%	72.5%

As summarized in Table 2, PIVOT Treatment B displayed reductions in the standard deviations of stress, mean stress as well as the maximum stress when compared to the initial beam at Iteration zero (0). These changes were achieved by the changing the internal geometry through the positioning of Voronoi sites without making any concessions in the volume (weight) of the beam.

Similar observations were noted for Case II as well. Throughout the 28 beams, a maximum of 28,727 nodal stresses and a minimum of 26,841 nodal stress were available for analysis. The results, at the end of nine (9) iterations,

from Case II are presented in Table 3. The initial base beam results, with standard deviation of stress of 23.82 MPa, mean stress of 27.18 MPa, and a maximum stress of 235.99 MPa, were considered as the 100 percent standards, and were compared with the output of the ninth iteration of respective techniques.

Table 3 Summary of nodal stress data after nine (9) iterations for Case II.

	Standard Deviation of Stress	Mean Stress	Maximum Stress
Lloyd's Algorithm	114.8%	103.5%	134.3%
PIVOT Treatment A	122.6%	116.1%	127.4%
PIVOT Treatment B	94.7%	90.6%	87.3%

PIVOT Treatment B showed evidence for structural optimization in Case II and Case III as well. Across the 28 beams, a maximum of 30,837 nodal stresses and a minimum of 27,287 nodal stress were available for analysis for Case III. The results at the end of nine (9) iterations are presented in Table 4. The initial base beam results, with standard deviation of stress of 27.05 MPa, mean stress of 29.51 MPa, and a maximum stress of 301.38 MPa, were considered as the 100 percent standards, and were compared with the results of the ninth iteration of three (3) techniques.

Table 4 Summary of nodal stress data after nine (9) iterations for Case III.

	Standard Deviation of Stress	Mean Stress	Maximum Stress
Lloyd's Algorithm	106.3%	101.5%	122.1%
PIVOT Treatment A	113.3%	115.6%	93.2%
PIVOT Treatment B	85.5%	88.4%	69.4%

Overall, across the three (3) Cases, PIVOT Treatment B was successful in reducing the standard deviation of stress while also lowering the mean stress as well as the maximum stress. The analysis of nodal stresses for all the 84 beams, with 28 unique beams in each case, was conducted to better understand and process the changes in the structural behavior of the members. A detailed summary of this analyzed data is made available in Appendix C.

The standard deviation of stress (in MPa) was graphically plotted against the iterations on the X-axis, to test for convergence. As evident from Figure 44, strong signs of convergence were displayed by the PIVOT Treatment B through the nine (9) iterations, irrespective of the initial starting Voronoi site distribution.

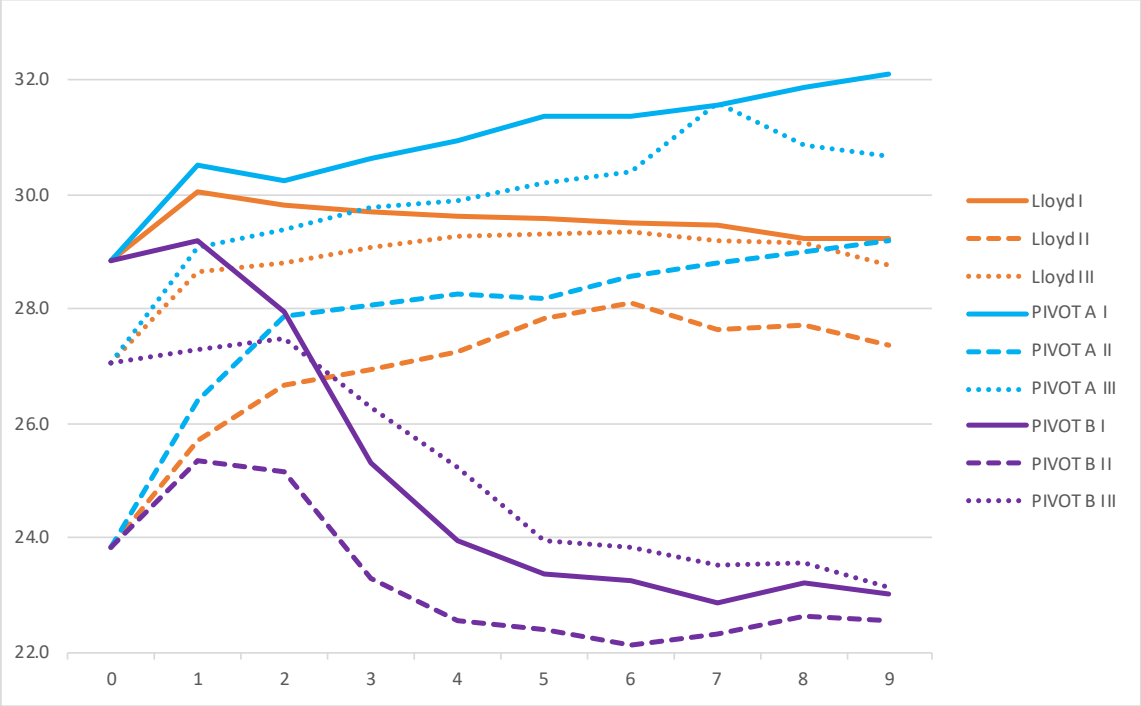

Figure 44 Test of convergence for reduction in standard deviation of stress.

At the end of nine iterations, the geometries obtained by the PIVOT Treatment A returned the highest standard deviation of stress for all three (3) cases followed by the Lloyd's algorithm. PIVOT Treatment B produced the lowest standard deviation of stress, spanning a bandwidth of 0.56 MPa, with the standard deviations of 23.03 MPa, 22.57 MPa and 23.13 MPa for Case I, Case II and Case III respectively for the nineth iteration. PIVOT Treatment A had the highest bandwidth of 2.89 MPa while the results from the Lloyd's algorithm spanned 1.87 MPa for the nineth iteration.

V.3 Hypothesis Testing

As mentioned in the Methodology chapter, three groups were created to test for the Hypothesis and determine if any statistically significant difference exists between the standard deviation of stress from the control and the treatments.

Group A (μ_A , σ_{A}, n_{A}), contained the output beams of PIVOT Treatment A such that μ_A was the mean of the standard deviation of stress from PIVOT Treatment A, σ_{A} was the standard deviation of the standard deviation of stress from PIVOT Treatment A, and n_{A} was the population of Group A. Similarly, Group B (μ_B , σ_{B}, n_{B}) and Group C (μ_C , σ_{C}, n_{C}) corresponding to PIVOT Treatment B and the Control – the Lloyd's algorithm respectively were also created. First, Group A (29.87, 2.05, 27) was tested against Group C (28.62, 1.23, 27) to determine whether any difference existed between the mean of the standard deviations of

stress between the PIVOT Treatment A and the Lloyd's algorithm. It can be stated with 95 percent confidence that the difference in the mean standard deviation of stress between the Lloyd's algorithm and PIVOT Treatment A is significant as evident from the following bounds calculated based on the collected data.

$$-1.93\ MPa\ \leq\ \bar{\mu}_{\mathrm{C}} - \bar{\mu}_{\mathrm{T}_A}\ \leq\ -0.56\ \mathrm{MPa}$$

Similarly, Group B (24.25, 3.68, 27) was tested against Group C (28.62, 1.23, 27) to determine whether any difference existed between the mean of the standard deviations of stress between the PIVOT Treatment B and the Lloyd's algorithm. It can be stated with 95 percent confidence that the difference in the mean standard deviation of stress between the Lloyd's algorithm and PIVOT Treatment B is also significant. The upper and lower bounds calculated for this comparison is as follows.

$$3.53\ MPa\ \leq\ \bar{\mu}_{\mathrm{C}} - \bar{\mu}_{\mathrm{T}_B}\ \leq\ 5.20\ \mathrm{MPa}$$

Since both the bounds comparing the means of Group A and Group C as well as the comparison between means of Group B and Groups C does not contain zero (0), for the given confidence interval, it is safe to reject the null hypothesis in the favor of the alternative hypothesis, that is $\bar{\mu}_{\mathrm{C}} - \bar{\mu}_{\mathrm{T}} \neq 0$. This implies that the PIVOT is significantly different from the Lloyd's algorithm with respect to the movement of Voronoi sites and their corresponding structural performance.

CHAPTER VI

DISCUSSIONS

This investigation was an attempt to determine whether geometry can impact the structural performance without alerting the volume (weight) of the structural members. As noted from the results, PIVOT Treatment B had favorable outcomes with regards to decreasing the stress concentrations as well as other parameters such as mean stress and maximum stress. Its performance was statistically significantly differently than the control and amounts to the novel contribution of this study.

VI.1 Study Outcomes

Two key study outcomes were achieved by this investigation. Foremost is the idea that potential reconfiguring of the Voronoi site to the regions of low stress, incorporated with the Extrusion scaffold, can help attain a better structural performance. This was the approach behind PIVOT Treatment B which stated that the new position of the Voronoi sites should be selected such that it is the stress-weighted centroid of the previous generation cell data, with the weights being inversely proportional to the stresses developed in their respective cells.

Since the Voronoi sites are encompassed by void, as it is defined by the Voronoi scaffold, moving this void towards regions of low stresses seems reasonable compared to moving the void to regions of high stresses. Thereby,

this strategic repositioning of material has shown the potential to lower the stresses for the same volume (weight), boundary conditions and loading conditions. Shown in Figure 45 is the output of the nineth iteration from Lloyd's algorithm for Case III. As this technique, which is independent of the structural performance, tends to uniformly distribute the Voronoi sites, the regularity in the cell size can be noted on the top face and the front face.

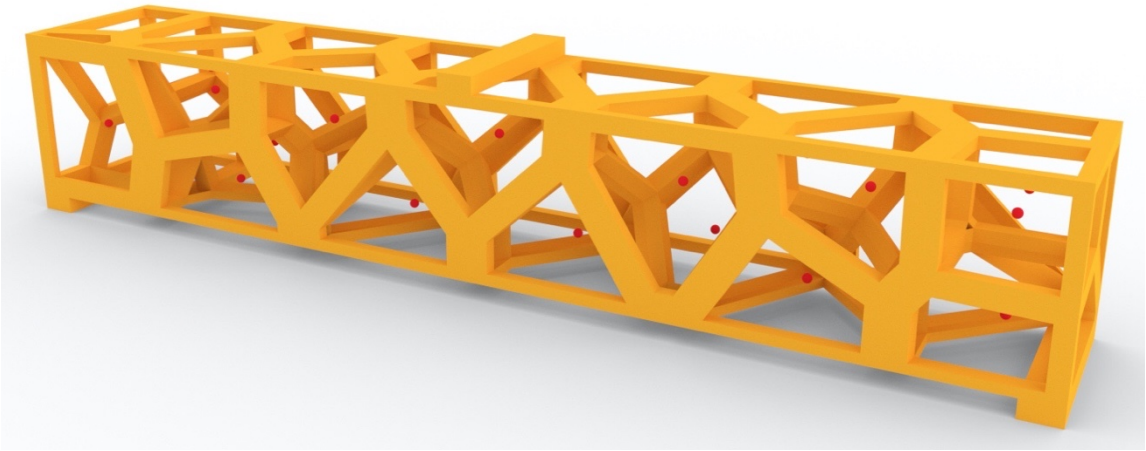

Figure 45 Voronoi sites and resulting beam from Lloyd's algorithm after nine iteration on Case III initial distribution.

Meanwhile, the output of the PIVOT treatments is dependent on the structural stresses as defined by the weights of the stress-weighted centroid. For PIVOT Treatment A, the Voronoi sites and the resulting structure of the nineth iteration for Case III, is shown in Figure 46. The weight was directly proportional to the stress value and as a result two cell layers can be seen below the loading strip. Similar observations were made in Case I and Case II as well.

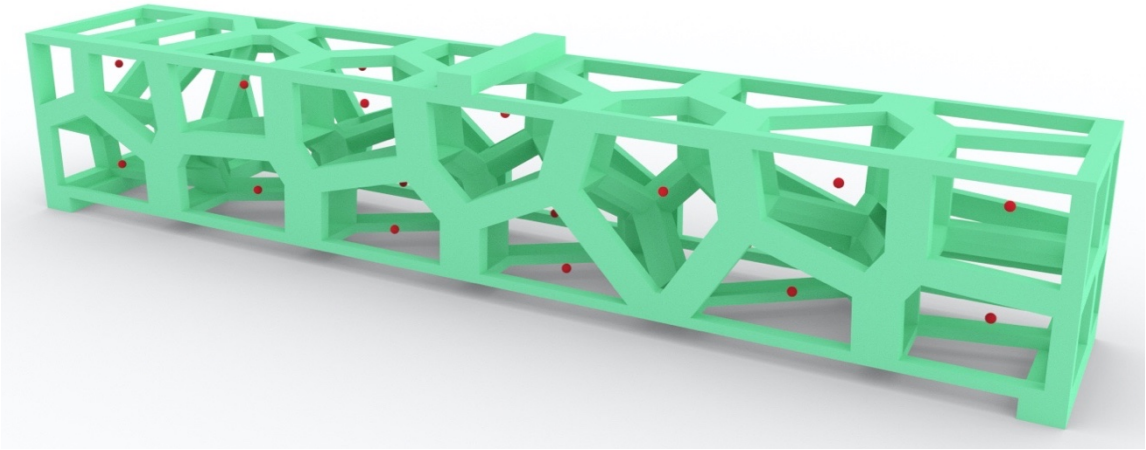

Figure 46 Voronoi sites and resulting beam from the nineth iteration of PIVOT Treatment A for Case III.

PIVOT Treatment B, where the weights were inversely proportional to the stresses, was designed such that the Voronoi sites move away from the regions of high stresses and towards the regions of low stresses. This is demonstrated in Figure 47 as a single layer of cell can be observed in the middle region below loading strip with multiple cell layers at both the horizontal ends.

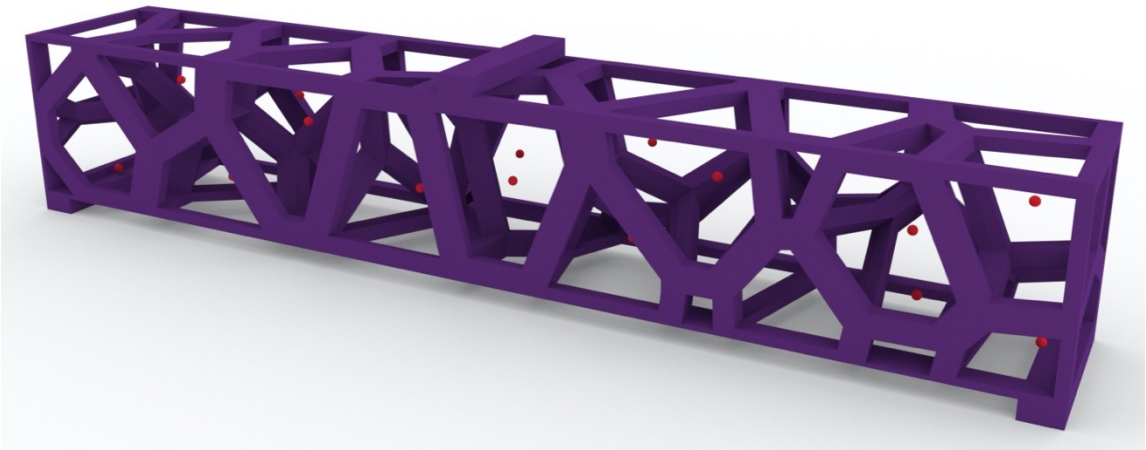

Figure 47 Nineth iteration output of PIVOT Treatment B for Case III.

In this investigation, a 100 N load was applied at the center of the top face of the beam. At the end of the nine (9) iterations, PIVOT Treatment B demonstrated a reduction in the maximum stress in all three (3) cases, ranging from 12 percent to 30 percent, as compared to the initial random distribution. In addition, the maximum stress for all the three (3) cases of PIVOT Treatment B was below the Tensile Yield Strength of stainless steel, which was not the case for the Lloyd's algorithm and PIVOT Treatment A. This implies that the output from PIVOT Treatment B can take more than 100 N load before reaching the Tensile Yield Strength. Given that all of the beams had the same weight, PIVOT Treatment B displays an increment in strength to weight ratio.

The second major insight from this study is the fundamental contribution towards identification of a directional movement regarding the position of the Voronoi sites in relation to the stress distribution. As stated in Chapter III, since the count of Voronoi sites was being kept constant, only option to determine the new position of the Voronoi sites was to switch or teleport them to new coordinates. A lack of information regarding the favorable vector direction for Voronoi sites, in relation to the structural performance, hindered the ability to translate the sites in 3D space.

Further detailed studies can help evaluate the potential routes for movement of Voronoi sites that can enhance structural performance. Achieving this will require a significant amount of testing and physical verification but can eventually help determine the optimal position for a given number of Voronoi sites.

Since PIVOT Treatment B successfully demonstrated improvements in the structural performance, the position of each successive iteration is visualized in the Figure 48 for Case I. The movement is depicted with help of the visual light spectrum (VIBGYOR) where violet dots denotes the position of Voronoi sites at the end of first iteration and red dots denotes the final position at the end of ninth iteration.

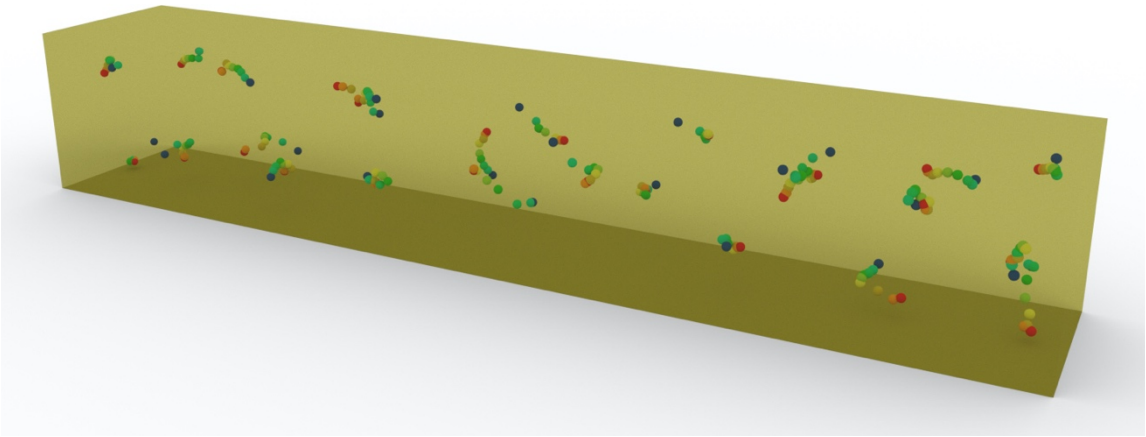

Figure 48 Movement of Voronoi sites in PIVOT Treatment B for Case I.

Similarly, the change in the position of Voronoi sites due to PIVOT Treatment B for Case II and Case III is visualized in Figure 49 and Figure 50 respectively. The red dots represent the positioning of the Voronoi sites for the ninth iteration. A majority of the sites showed significant change in position including some with rough directional changes in the routes across the three (3) cases. There were also a few sites that did not undergo much movement.

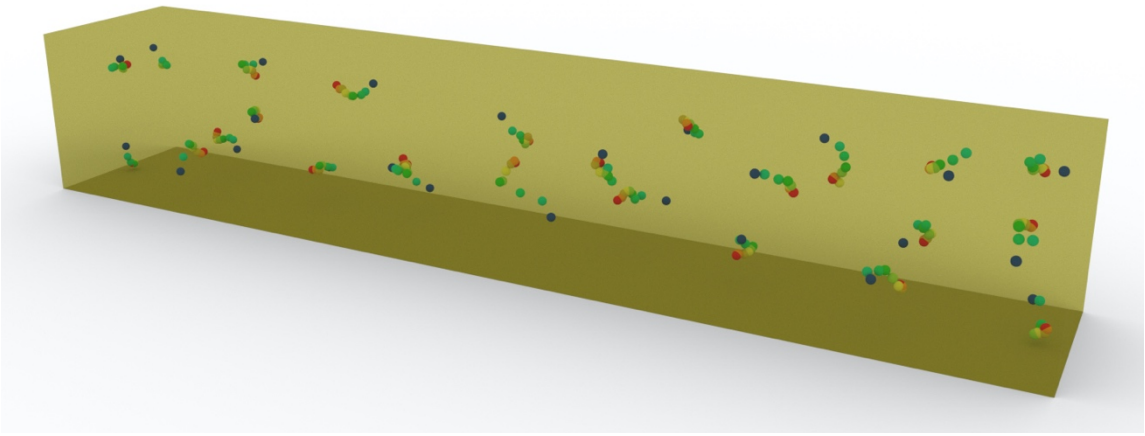

Figure 49 Movement of Voronoi sites in PIVOT Treatment B for Case II.

However, it is worth noting that the Voronoi tessellation obtained in this study is generated at the bisectors of the Voronoi sites, and therefore, the change in form is dependent on the movement of the bisectors. For instance, if the movement of two neighboring Voronoi sites happens to be symmetric about the bisecting face, edge or point, then the bisector and subsequent form will not change despite the change in the position of the Voronoi sites.

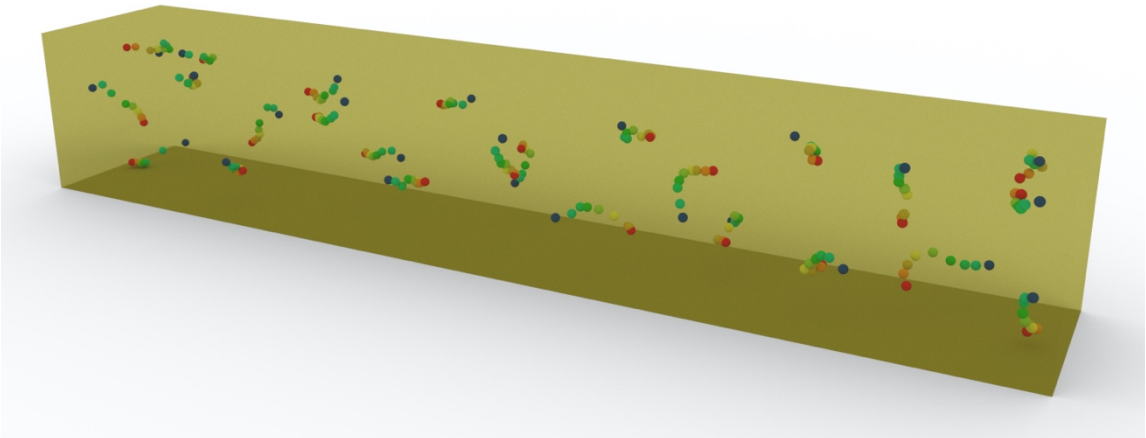

Figure 50 Movement of Voronoi sites in PIVOT Treatment B for Case III.

An evaluation of the final distribution, that is the ninth iteration, of the 25 Voronoi sites across the three cases, for a combined total of 75 sites, presents an enhanced view on the workings of the techniques as seen in Figure 51. This figure displays the front and side view of the beam, and the spread of Voronoi sites across the optimization domain. The middle third of the front view of the beam is shaded green to illustrate the region with the loading strip. Iteration 0 sites are shown in black and Iteration 9 sites are displayed in red.

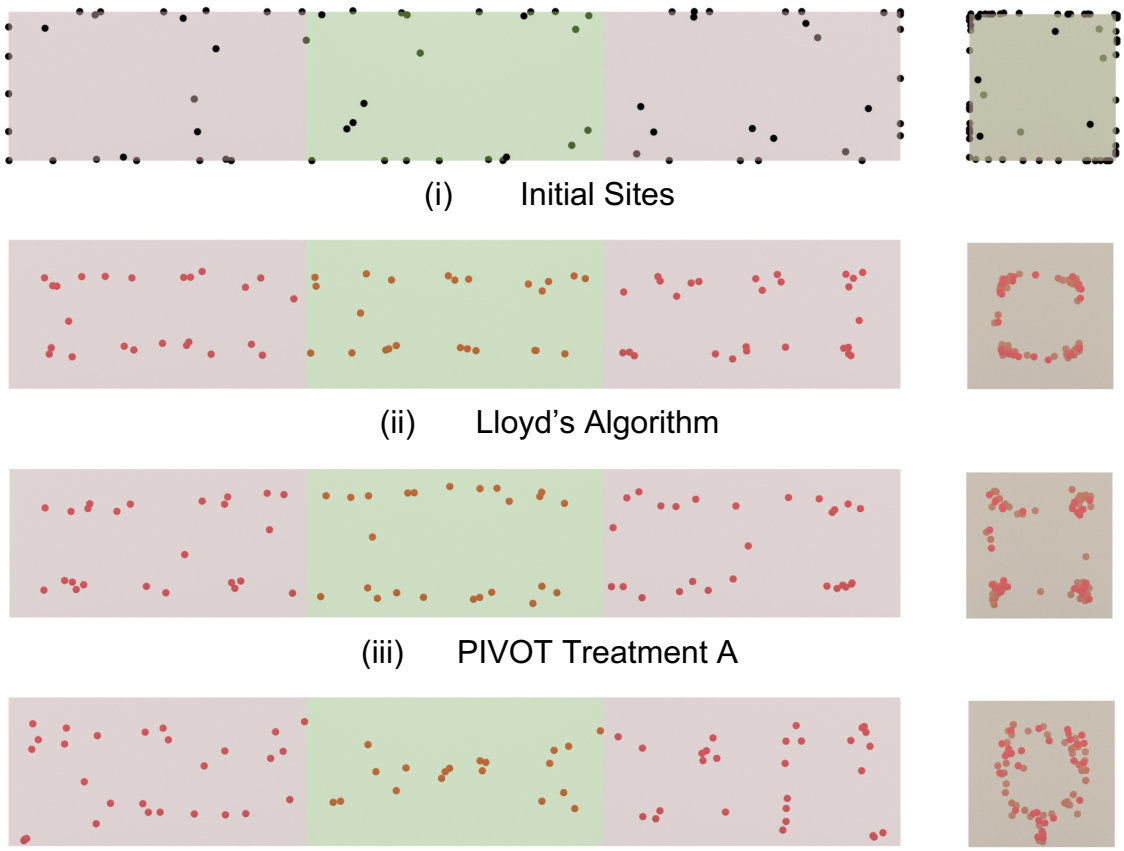

Figure 51 The Front view (left) and Side view (right) of all sites across the three cases.

A noticeable difference can be observed in the distribution of the Voronoi sites. A majority of the Voronoi sites, during the initial random starting solution, were place on or very close to the periphery. The Lloyd's algorithm, through the nine (9) iterations, is able to reorganize the sites such that they display an even distance from the boundaries across the three regions as seen in the front view. The front view of the sites from PIVOT Treatment A, while not on the edges, but are relatively closer to the edges as compared to the Lloyd's algorithm. This is more pronounced in the green shaded region (middle third) where the stress concentrations were visible in the structural analysis.

Compared to the other distributions, the output of PIVOT Treatment B has noticeable reduction of Voronoi sites, about 16 percent less, in the middle region. Also, the sites are concentrated far away from both the edges in the green region. However, the bottom face on the outside thirds, did have some sites near the edges as noticeable from the side view.

In addition to evaluating the movement of the Voronoi sites and the stress distribution, another important criterion was closely monitored. In many instances, the structural optimization problem is formulated as the minimization of the strain energy as introduced by Bendsøe and Kikuchi (1988), and followed in the SIMP method. A minimization of the strain energy corresponds to the maximization of stiffness. Therefore, the total strain energy was also collected during this investigation to verify the results. PIVOT Treatment B nineth beam showed a notable reduction of the total strain energy, 10 – 18 percent less as compared to

the initial beam. Meanwhile, the other two techniques, Lloyd's algorithm and PIVOT Treatment A, failed to show any reduction in the strain energy. A comparison is depicted in Figure 52, where the total strain energy (in milli Joules) is mapped on the Y-axis and the iterations are shown on the X-axis. In case of PIVOT Treatment A, an increase of 21 – 33 percent was recorded in the total strain energy as compared to the total strain energy of the initial zero (0) beam while the Lloyd's algorithm showed a 1 – 17 percent increase. This further supports the notion that PIVOT Treatment B is a viable approach for exploring and furthering efforts in structural optimization. The details corresponding to this figure can be found in Appendix C.

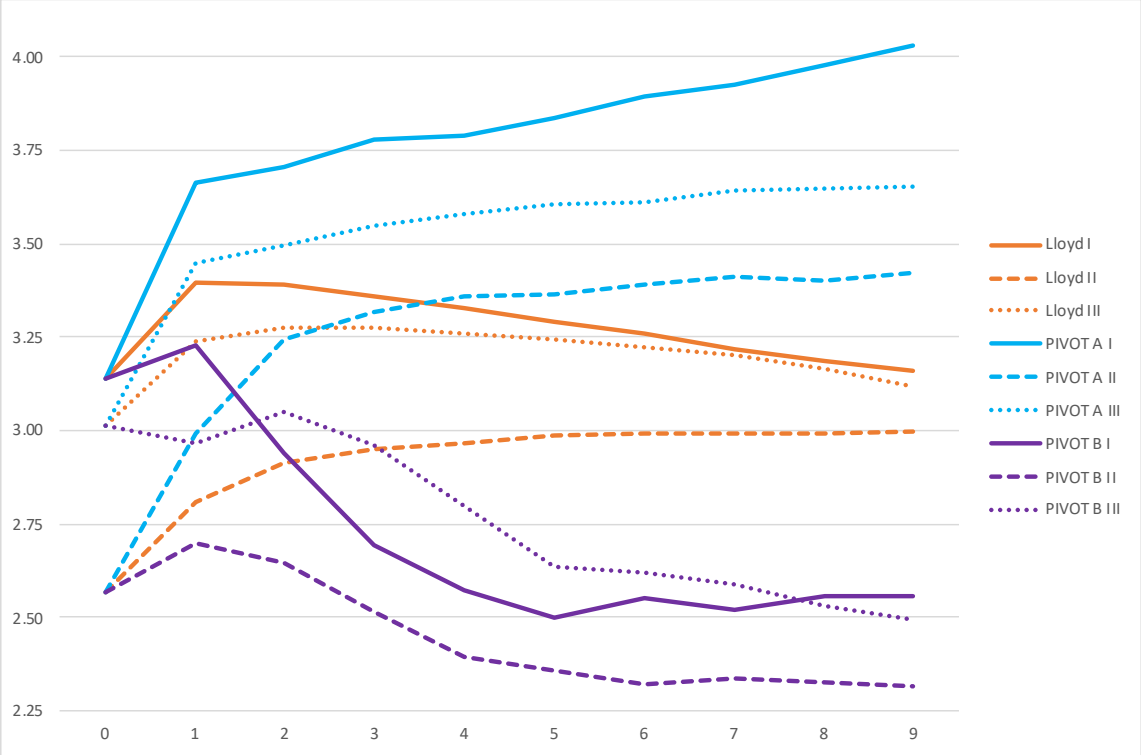

Figure 52 Total strain energy of the beams over nine iterations.

VI.2 Current Challenges

The current investigation was developed with the position of Voronoi sites as the independent variable and the structural performance as the dependent variable. While the PIVOT Treatment B performance seems to be independent of the initial distribution of the Voronoi sites, several other parameters were fixed so that they do not interfere with the outcomes. The list of such parameters include the count of Voronoi sites, which was fixed to 25 for this study, the boundary and loading conditions that were set to the typical MBB beam setup, the Voronoi scaffold which was set to the Extrusion scaffold while the porosity of the beam was 85 percent throughout this investigation.

Additional studies need to be conducted to determine whether PIVOT Treatment B can improve structural performance throughout the full range of the other parameters that were fixed for this investigation. Meanwhile, the time expense associated with reaching convergence will also need to be evaluated.

Furthermore, this approach will need adjustments to deal with free-form geometries and to determine robust methods to clip the Voronoi tessellation and scaffold inside the free-form geometry as depicted in Figure 53. Also, presently the scope was limited to internal form-finding, however, the extension to a simultaneous internal and external form-finding presents many challenges and new opportunities. In addition, the issues related to Explicit Geometry Union will need to be addressed. Potential fabrication and multi-material manufacturing, for

non-linear materials, can also present many significant challenges that will certainly require additional modifications to this technique.

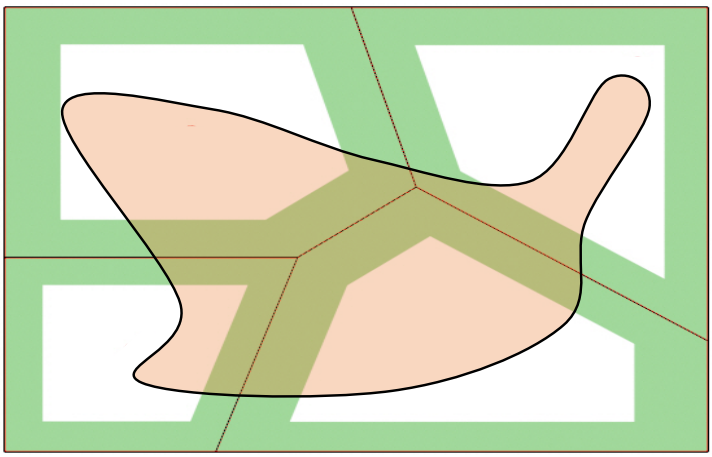

Figure 53 Depiction of challenge associated with clipping Voronoi scaffold to free-form geometries.

VI.3 Future Scope

The current investigation was conducted at a very fundamental level to understand the intricate details and mechanics of the load transfer behavior, made possible due to the fabrication enhancements offered by additive manufacturing. Extensive physical evaluations and verifications will be required before any practical applications takes shape. However, upon successful completion, this technique can be applied extensively in architecture, engineering and construction industries. Figure 54 as adopted from Yadav (2020) is an additively manufactured modular arch structure where the internal members were obtained from a Voronoi tessellation. Based on the design intent and application of such modular arches,

such as for emergency shelter vaults or affordable housing, the boundary and loading conditions can be simulated to enhance their performance using PIVOT. Similarly Figure 55 is a rendering of a chair design that can potentially utilize PIVOT to produce an optimal internal structure.

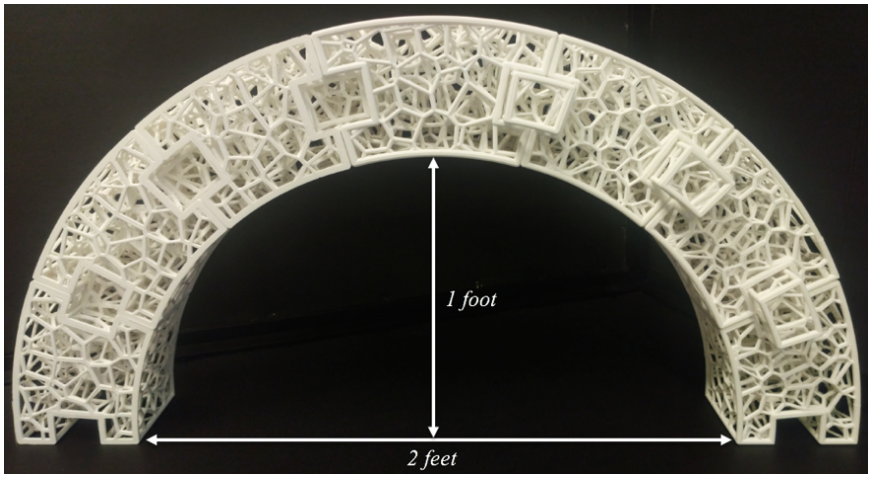

Figure 54 Lightweight modular structure with internal Voronoi tessellation as adopted from Yadav (2020).

Figure 55 A Voronoi tessellation featured chair rendering.

CHAPTER VII

CONCLUSIONS AND RECOMMENDATIONS

This investigation was conducted in relation to Level Two of light-weighting that has been achieved due to the fabrication advancements offered by additive manufacturing. More specifically, the research question posed here was to determine whether we can utilize Level Two light-weighting such that all internal structural members develop same amount of stress without making any changes to the volume (weight) and the external boundaries.

To answer this particular research question, a novel parametric technique was proposed based on a bioinspired mathematical formulation, the Voronoi tessellation. It is a concept that helps divide space based on its proximity from certain key points. The field of interest for this study was to identify key Voronoi sites to manipulate structural performance but more specifically to reduce and remove concentrations of high stresses. This attempt was made by repositioning the material through iterative feedback from the structural performance rather than changing the net volume.

The proposed novel algorithm utilized stress-weighted centroids of Voronoi tessellation to identify the next set of Voronoi sites near regions of either low or high stresses, depending on the weight definition, to rearrange the voids. Subsequently, the material is strategically redistributed around those void spaces. Hence, two weights were formulated, one directly proportional to the stresses,

Treatment A, and another one inversely proportional to the stresses, Treatment B. Since the objective was to achieves a more uniform stress distribution, a Control, the Lloyd's algorithm was selected as the performance baseline.

The null research hypothesis was formulated to state that there will be no significant difference between the standard deviation of stress obtained from the beams corresponding to Voronoi sites as determined by the control, which is a strictly geometric computation, and the treatments, which are stress-weighted computations. A methodology was adopted to test the alternative hypothesis stating a statistically significant difference in the standard deviation of stress between the control and treatment techniques on a 3D full MBB beam.

This research objective was met through computational simulations to conduct static structural analysis. Three (3) different starting distributions of 25 Voronoi sites were evaluated over nine (9) iterations for each of the techniques. The investigation results indicate that both the treatment techniques, with weights directly proportional to the stresses and weights inversely proportional to the stresses, were statistically significantly different from the control. Based on the 95 percent confidence in the results, this investigation recommends rejecting the null hypothesis in favor of the alternative hypothesis.

Moreover, the proposed PIVOT treatment, with weights inversely proportional to the stresses, showed positive signs of convergence irrespective of the starting distribution of the Voronoi sites. Furthermore, through nine (9) iterations, it demonstrated 05 to 30 percent reduction in the standard deviation of

stress along with 09 to 11 percent decrease in the mean stress while lowering the maximum stress value by 12 to 30 percent. The improvements in structural performance were achieved by repositioning of material and the internal geometry without altering the net volume (weight) or the external boundary. Hence, the research question posed in this investigation was answered affirmatively that Level Two light-weighting can be utilized to improve the uniformity of stress across the internal structural members.

Future studies should be designed to test the impact of changes in porosity, scaffold selection, count of Voronoi sites and the ability to enhance the structural performance for various boundary and loading conditions. Additionally, since the scope of this investigation did not include direct comparisons with lattice structures or space-frame trusses, further research needs to be conducted to evaluate the performance of the technique introduced in this study against those solutions and other generative design techniques.

The outcomes of this investigation suggest that using stress-weighted centroids for Voronoi tessellation is a promising approach to improve the structural performance as noted by the reductions of the standard deviations of stress, mean stress and maximum stress value while achieving high porosity. It provides the warrant for further detailed studies and the need for physical testing and verifications to make adjustments and improvements to the algorithm. Furthermore, as Level Two light-weighting becomes prevalent and economically feasible, PIVOT has the potential to play an essential role in understanding and

harvesting geometric form in relation to the mechanical performance while being helpful for the ecology and enriching the current intellectual efforts in context of optimization of the structural form.

Additionally, parallel studies to better understand the role of Voronoi tessellation in Nature can also help redefine and adjust the weight definitions beyond the two treatments presented in this investigation. Detailed studies on the relationship of the structural performance of bones, geological rocks and metallurgy grains with the underlying Voronoi tessellation can certainly provide a major boost to advance the technique presented here. Additionally, living material such as bones have the capabilities to alter their mass density over time. Studying the movement of corresponding Voronoi sites can also open new endeavors to design structures that actively react to the local boundary and loading conditions while utilizing the advancements in material sciences and the creativity of Nature.

REFERENCES

Abambres, M., Rajana, K., Tsavdaridis, K. D., Ribeiro, T. P. 2019. Neural Network-Based Formula for the Buckling Load Prediction of I-Section Cellular Steel Beams. *Computers*, 8(1): 2.

Addis, B. 2006. The Crystal Palace and Its Place in Structural History. *International Journal of Space Structures*, 1: 3-19.

Al Rashid, A., Khan, S. A., G. Al-Ghamdi, S., Koç, M. 2020. Additive Manufacturing: Technology, Applications, Markets, and Opportunities for the Built Environment. *Automation in Construction*, 118: 103268.

Al-Ketan, O., Rowshan, R., Abu Al-Rub, R. K. 2018. Topology-Mechanical Property Relationship of 3d Printed Strut, Skeletal, and Sheet Based Periodic Metallic Cellular Materials. *Additive Manufacturing*, 19: 167-183.

Allaire, G., Bonnetier, E., Francfort, G., Jouve, F. 1997. Shape Optimization by the Homogenization Method. *Numerische Mathematik*, 76: 27-68.

Allaire, G., Schoenauer, M. 2007. *Conception Optimale De Structures,* Springer, Berlin.

Allaire, G., Geoffroy-Donders, P., Pantz, O. 2019. Topology Optimization of Modulated and Oriented Periodic Microstructures by the Homogenization Method. *Computers & Mathematics with Applications*, 78: 2197-2229.

Ash, P. F., Bolker, E. D. 1985. Recognizing Dirichlet Tessellations. *Geometriae Dedicata*, 19: 175-206.

Audibert, C., Chaves-Jacob, J., Linares, J.-M., Lopez, Q.-A. 2018. Bio-Inspired Method Based on Bone Architecture to Optimize the Structure of Mechanical Workspieces. *Materials and Design*, 160: 708-717.

Bank, L. C., Bednarczyk., P. J. 1988. A Beam Theory for Thin-Walled Composite Beams. *Composites Science and Technology*, 32: 265-277.

Bendsøe, M. P., Kikuchi, N. 1988. Generating Optimal Topologies in Structural Design Using a Homogenization Method. *Computer Methods in Applied Mechanics and Engineering*, 71(2): 197-224.

Bendsøe, M. P. 1989. Optimal Shape Design as a Material Distribution Problem. *Structural Optimization*, 1: 193-202.

Bourdin, B., Chambolle, A. 2006. The Phase-Field Method in Optimal Design. In *IUTAM Symposium on Topological Design Optimization of Structures, Machines and Materials*, Dordrecht, Netherlands.

Burger, M., Hackl, B., Ring, W. 2004. Incorporating Topological Derivatives into Level Set Methods. *Journal of Computational Physics*, 194: 344-362.

Cucinotta, F., Raffaele, M., Salmeri, F. 2019. A Stress-Based Topology Optimization Method by a Voronoi Tessellation Additive Manufacturing Oriented. *The International Journal of Advanced Manufacturing Technology*, 103: 1965-1975.

Delaunay, B. 1934. Sur La Sphere Vide. *Izv. Akad. Nauk SSSR, Otdelenie Matematicheskii i Estestvennyka Nauk*, 7: 1-2.

Descartes, R. 1644. *Principia Philosophiae*, Apud Ludovicum Elzevirium, Amsterdam.

Du, Q., Faber, V., Gunzburger, M. 1999. Centroidal Voronoi Tessellations: Applications and Algorithms. *SIAM Review*, 41: 637-676.

Du, Y., Liang, H., Xie, D., Mao, N., Zhao, J., Tian, Z., Wang, C., Shen, L. 2019. Finite Element Analysis of Mechanical Behavior, Permeability of Irregular Porous Scaffolds and Lattice-Based Porous Scaffolds. *Materials Research Express*, 6(10): 105407.

Du, Y., Liang, H., Xie, D., Mao, N., Zhao, J., Tian, Z., Wang, C., Shen, L. 2020. Design and Statistical Analysis of Irregular Porous Scaffolds for Orthopedic Reconstruction Based on Voronoi Tessellation and Fabricated Via Selective Laser Melting (SLM). *Materials Chemistry and Physics*, 239: 121968.

Edison, T. A. 1917. Process of Constructing Concrete Buildings. U.S. Patent No. 1,219,272.

Eschenauer, H. A., Kobelev, V. V., Schumacher, A. 1994. Bubble Method for Topology and Shape Optimization of Structures. *Structural Optimization*, 8: 42-51.

Feng, J., Fu, J., Lin, Z., Shang, C., Li, B. 2018. A Review of the Design Methods of Complex Topology Structures for 3d Printing. *Visual Computing for Industry, Biomedicine, and Art*, 1(1): 1-16.

Fleury, C., Braibant, V. 1986. Structural Optimization: A New Dual Method Using Mixed Variables. *International Journal for Numerical Methods in Engineering*, 23: 409-428.

Gain, A. L., Paulino, G. H., Duarte, L. S., Menezes, I. F. 2015. Topology Optimization Using Polytopes. *Computer Methods in Applied Mechanics and Engineering*, 293: 411-430.

Gao, R., Li, D., Dong, L., Wang, X. 2019. Numerical Analysis of the Mechanical Properties of 3D Random Voronoi Structures with Negative Poisson's Ratio. *Physica Status Solidi (b)*, 256(7): 1800539.

Ghosh, S. 2011. *Micromechanical Analysis and Multi-Scale Modeling Using the Voronoi Cell Finite Element Method*, CRC Press, Boca Raton.

Gomez, S., Vlad, M. D., Lopez, J., Fernandez, E. 2016. Design and Properties of 3D Scaffolds for Bone Tissue Engineering. *Acta Biomaterialia*, 42: 341-350.

Huber, N. 2018. Connections between Topology and Macroscopic Mechanical Properties of Three-Dimensional Open-Pore Materials. *Frontiers in Materials*, 5: 69.

Kohnke, P. 1982. Ansys. In *Finite Element Systems*, 19-25, Springer, Berlin Heidelberg.

Leary, M., Merli, L., Torti, F., Mazur, M., Brandt, M. 2014. Optimal Topology for Additive Manufacture: A Method for Enabling Additive Manufacture of Support-Free Optimal Structures. *Materials and Design*, 63: 678-690.

Lee, M., Fang, Q., Cho, Y., Ryu, J., Liu, L., Kim, D.-S. 2018. Support-Free Hollowing for 3D Printing Via Voronoi Diagram of Ellipses. *Computer-Aided Design*, 101: 23-36.

Li, D., Liao, W., Dai, N., Dong, G., Tang, Y., Xie, Y. M. 2018. Optimal Design and Modeling of Gyroid-Based Functionally Graded Cellular Structures for Additive Manufacturing. *Computer-Aided Design*, 104: 87-99.

Liu, J., Gaynor, A. T., Chen, S., Kang, Z., Suresh, K., Takezawa, A., Li, L., et al. 2018. Current and Future Trends in Topology Optimization for Additive Manufacturing. *Structural and Multidisciplinary Optimization*, 57: 2457-2483.

Lloyd, S. 1982. Least Squares Quantization in PCM. *IEEE Transactions on Information Theory*, 28: 129-137.

Lu, L., Sharf, A., Zhao, H., Wei, Y., Fan, Q., Chen, X., Savoye, Y., Tu, C., Cohen-Or, D., Chen, B. 2014. Build-to-Last. *ACM Transactions on Graphics*, 33: 1-10.

Mandelbrot, B. 2013. *Fractals and Chaos: The Mandelbrot Set and Beyond*, Springer Science and Business Media, Berlin.

Martin, R. B. 2007. The Importance of Mechanical Loading in Bone Biology and Medicine. *Journal of Musculoskeletal and Neuronal Interactions*, 7: 48.

Martínez, J., Dumas, J., Lefebvre, S. 2016. Procedural Voronoi Foams for Additive Manufacturing. *ACM Transactions on Graphics*, 35: 1-12.

Martínez, J., Hornus, S., Song, H., Lefebvre, S. 2018. Polyhedral Voronoi Diagrams for Additive Manufacturing. *ACM Transactions on Graphics*, 37: 1-15.

Martínez, J., Skouras, M., Schumacher, C., Hornus, S., Lefebvre, S., Thomaszewski, B. 2019. Star-Shaped Metrics for Mechanical Metamaterial Design. *ACM Transactions on Graphics*, 38: 1-13.

McNeel, R. 2015. Rhinoceros. *NURBS modleing for Windows*. Retrieved 5th April 2021 from https://www.rhino3d.com/.

Michell, A. G. M. 1904. LVIII. The Limits of Economy of Material in Frame-Structures. *The London, Edinburgh, and Dublin Philosophical Magazine and Journal of Science*, 8: 589-597.

Misztal, M. K., Bærentzen, J. A. 2012. Topology-Adaptive Interface Tracking Using the Deformable Simplicial Complex. *ACM Transactions on Graphics*, 31: 1-12.

Molotnikov, A., Simon, G. P., Estrin, Y. 2019. Architectured Polymeric Materials Produced by Additive Manufacturing. In *Architectured Materials in Nature and Engineering,* 257-285, Springer, Cham.

MX3D, B. V. 2018. Mx3d Bridge. Retrieved 5th April 2021 from https://mx3d.com/projects/mx3d-bridge/.

Nematollahi, B., Xia, M., Sanjayan, J. 2017. Current Progress of 3D Concrete Printing Technologies. In *ISARC Proceedings of the International Symposium on Automation and Robotics in Construction*, Taipei, Taiwan.

Osher, S., Sethian, J. A. 1988. Fronts Propagating with Curvature-Dependent Speed: Algorithms Based on Hamilton-Jacobi Formulations. *Journal of Computational Physics*, 79: 12-49.

Panesar, A., Abdi, M., Hickman, D., Ashcroft, I. 2018. Strategies for Functionally Graded Lattice Structures Derived Using Topology Optimisation for Additive Manufacturing. *Additive Manufacturing*, 19: 81-94.

Picelli, R., Townsend, S., Brampton, C., Norato, J., Kim, H. A. 2018. Stress-Based Shape and Topology Optimization with the Level Set Method. *Computer Methods in Applied Mechanics and Engineering*, 329: 1-23.

Plocher, J., Panesar, A. 2019. Review on Design and Structural Optimisation in Additive Manufacturing: Towards Next-Generation Lightweight Structures. *Materials and Design*, 183: 108164.

Pokojski, W., Pokojska, P. 2018. Voronoi Diagrams – Inventor, Method, Applications. *Polish Cartographical Review*, 50: 141-150.

Prager, W., Taylor, J. E. 1968. Problems of Optimal Structural Design. *Journal of Applied Mechanics*, 35(1): 102-106.

Querin, O. M., Steven, G. P., Xie, Y. M. 1998. Evolutionary Structural Optimisation (ESO) Using a Bidirectional Algorithm. *Engineering Computations*, 15: 1031-1048.

Ramadani, R., Belsak, A., Kegl, M., Predan, J., Pehan, S. 2018. Topology Optimization Based Design of Lightweight and Low Vibration Gear Bodies. *International Journal of Simulation Modelling*, 17: 92-104.

Rozvany, G. 1972. Grillages of Maximum Strength and Maximum Stiffness. *International Journal of Mechanical Sciences*, 14: 651-666.

Rozvany, G., Zhou, M. 1991. The Coc Algorithm, Part I: Cross-Section Optimization or Sizing. *Computer Methods in Applied Mechanics and Engineering*, 89: 281-308.

Rutten, D. 2015. Grasshopper3D. Retrieved 5th April 2021 from https://www.grasshopper3d.com/.

Ryan, T. M., Walker, A. 2010. Trabecular Bone Structure in the Humeral and Femoral Heads of Anthropoid Primates. *The Anatomical Record: Advances in Integrative Anatomy and Evolutionary Biology,* 293(4): 719-729.

Sigmund, O. 2001. A 99 Line Topology Optimization Code Written in Matlab. *Structural and Multidisciplinary Optimization*, 21: 120-127.

Sullivan, T. N., Wang, B., Espinosa, H. D., Meyers, M. A. 2017. Extreme Lightweight Structures: Avian Feathers and Bones. *Materials Today*, 20: 377-391.

Svanberg, K. 1987. The Method of Moving Asymptotes—a New Method for Structural Optimization. *International Journal for Numerical Methods in Engineering*, 24: 359-373.

Thompson, D. W. 1917. On Growth and Form, Cambridge University Press, London.

Torres, A. M., Trikanad, A. A., Aubin, C. A., Lambers, F. M., Luna, M., Rimnac, C. M., Zavattieri, P., Hernandez, C. J. 2019. Bone-Inspired Microarchitectures Achieve Enhanced Fatigue Life. *Proceedings of the National Academy of Sciences of the United States of America,* 116: 24457-24462.

Tsavdaridis, K. D., Kingman, J. J., Toropov, V. V. 2015. Application of Structural Topology Optimisation to Perforated Steel Beams. *Computers and Structures*, 158: 108-123.

Tyflopoulos, E., Tollnes, F. D., Steinert, M., Olsen, A. 2018. State of the Art of Generative Design and Topology Optimization and Potential Research Needs. In *DS 91: Proceedings of NordDesign 2018,* Linköping, Sweden.

Van Miegroet, L., Duysinx, P. 2007. Stress Concentration Minimization of 2d Filets Using X-Fem and Level Set Description. *Structural and Multidisciplinary Optimization*, 33: 425-438.

Voronoi, G. 1908. Nouvelles Applications Des Paramètres Continus À La Théorie Des Formes Quadratiques. Deuxième Mémoire. Recherches Sur Les Parallélloèdres Primitifs. *Journal für die reine und angewandte Mathematik*, 1908: 198-287.

Wang, C., Qian, X. 2020. A Density Gradient Approach to Topology Optimization under Design-Dependent Boundary Loading. *Journal of Computational Physics*, 411: 109398.

Wang, G., Shen, L., Zhao, J., Liang, H., Xie, D., Tian, Z., Wang, C. 2018. Design and Compressive Behavior of Controllable Irregular Porous Scaffolds: Based on Voronoi-Tessellation and for Additive Manufacturing. *ACS Biomaterials Science and Engineering*, 4: 719-727.

Wang, W., Munro, D., Wang, C. C. L., van Keulen, F., Wu, J. 2020. Space-Time Topology Optimization for Additive Manufacturing. *Structural and Multidisciplinary Optimization*, 61: 1-18.

Wu, J., Wang, C. C. L., Zhang, X., Westermann, R. 2016. Self-Supporting Rhombic Infill Structures for Additive Manufacturing. *Computer-Aided Design*, 80: 32-42.

Wu, J., Aage, N., Westermann, R., Sigmund, O. 2017. Infill Optimization for Additive Manufacturing—Approaching Bone-Like Porous Structures. *IEEE Transactions on Visualization and Computer Graphics*, 24: 1127-1140.

Wu, J., Wang, W., Gao, X. 2019. Design and Optimization of Conforming Lattice Structures. *IEEE Transactions on Visualization and Computer Graphics*, 27: 43-56.

Yadav, N. 2020. Interlocking Vaults by Voronoi Decomposition of 3D Space. In *Shape Modeling International 2020 Fabrication and Sculpting Event (FASE),* Strasbourg, France.

Zhang, H., Ding, X., Dong, X., Xiong, M. 2018. Optimal Topology Design of Internal Stiffeners for Machine Pedestal Structures Using Biological Branching Phenomena. *Structural and Multidisciplinary Optimization*, 57: 2323-2338.

Zhong, T., He, K., Li, H., Yang, L. 2019. Mechanical Properties of Lightweight 316l Stainless Steel Lattice Structures Fabricated by Selective Laser Melting. *Materials and Design*, 181: 108076.

Zhou, M., Rozvany, G. 1991. The Coc Algorithm, Part II: Topological, Geometrical and Generalized Shape Optimization. *Computer methods in applied mechanics and engineering*, 89: 309-336.

Zhou, M., Rozvany, G. 2001. On the Validity of Eso Type Methods in Topology Optimization. *Structural and Multidisciplinary Optimization*, 21: 80-83.

APPENDIX A

POROUS VORONOI SCAFFOLD

The four approaches mentioned in III.1 were compared for 5 Voronoi sites in a 10 x 10 x 10 box (total volume 1000 unit^3). 10 such set with various distribution of the 5 Voronoi sites were evaluated to determine the efficiency of the approaches. The chosen platform for the comparison was *Rhinoceros 7* and the graphical codes were setup in *Grasshopper3D* interface within the *Rhinoceros 7* workspace. For the cases where the Boolean operation failed in *Grasshopper3D*, an attempt was made in the *Rhinoceros 7* workspace.

Table A1 Computational details of Cylindrical scaffold approach.

Voronoi Site Set {Sites = 5}	Total Run Time (seconds)	Boolean Union Operation		Success	Success Run Time (seconds)	Resulting Volume
		Grasshopper	Rhinoceros			
1	7.1	Success		Yes	7.1	199.8
2	4.4	Fail	Success	Yes	4	199.7
3	8.1	Success	-	Yes	8.1	197.7
4	7.6	Fail	Fail	No	-	
5	7.9	Success	-	Yes	7.9	197.2
6	3.2	Fail	Fail	No	-	
7	8	Success	-	Yes	8	209.3
8	1	Fail	Fail	No	-	
9	9.4	Success	-	Yes	9.4	196
10	8.5	Success	-	Yes	8.5	202.7
				70%	7.6	4.5 (Deviation)

The Procedural scaffold did not return any result for the Boolean Union, but the total volume was computed as the cumulative sum of the included voxels.

Table A2 Computational details of Procedural scaffold approach.

Voronoi Site Set {Sites = 5}	Total Run Time (seconds)	Boolean Union Operation		Success	Success Run Time (seconds)	Resulting Volume
		Grasshopper	Rhinoceros			
1	8	Fail	Fail	No	-	200.1
2	5.9	Fail	Fail	No	-	200.8
3	10.4	Fail	Fail	No	-	198.1
4	8.5	Fail	Fail	No	-	191.6
5	9.2	Fail	Fail	No	-	196.5
6	6.4	Fail	Fail	No	-	207.1
7	6.8	Fail	Fail	No	-	212.5
8	9.6	Fail	Fail	No	-	201.7
9	9.2	Fail	Fail	No	-	199.5
10	7.5	Fail	Fail	No	-	202.3
				0%	-	5.7 (Deviation)

Table A3 Computational details of Extrusion scaffold approach.

Voronoi Site Set {Sites = 5}	Total Run Time (seconds)	Boolean Union Operation		Success	Success Run Time (seconds)	Resulting Volume
		Grasshopper	Rhinoceros			
1	< 1	Success	-	Yes	< 1	199.8
2	<1	Success	-	Yes	<1	199.8
3	< 1	Success	-	Yes	< 1	199.8
4	< 1	Success	-	Yes	< 1	199.8
5	< 1	Success	-	Yes	< 1	199.8
6	< 1	Success	-	Yes	< 1	199.8
7	< 1	Success	-	Yes	< 1	199.8
8	< 1	Success	-	Yes	< 1	199.8
9	< 1	Success	-	Yes	< 1	199.8
10	< 1	Success	-	Yes	< 1	199.8
				100%	<1	2.9959E-14 (Deviation)

Similar to the Procedural scaffold, the resulting volume of the Dirinoi scaffold is the cumulative volume of the lower order Brep from the site point collection. It was determined by simple summation of those Brep, for all cases including the ones that failed the Boolean Union operation and was verified for successful Boolean operations.

Table A4 Computational details of Dirinoi scaffold approach.

Voronoi Site Set {Sites = 5}	Total Run Time (seconds)	Boolean Union Operation		Success	Success Run Time (seconds)	Resulting Volume
		Grasshopper	Rhinoceros			
1	9	Fail	Fail	No	-	200
2	15.2	Fail	Fail	No	-	198.6
3	23	Fail	Success	Yes	23	197.4
4	29.9	Fail	Success	Yes	29.9	198.2
5	21	Fail	Fail	No	-	198.3
6	27.4	Fail	Success	Yes	27.4	202
7	10.9	Fail	Fail	No	-	204.4
8	15.2	Fail	Fail	No	-	200.3
9	23.7	Fail	Fail	No	-	197.6
10	23.1	Fail	Success	Yes	23.1	199.5
				40%	25.9	2.2 (Deviation)

APPENDIX B

STRUCTURAL ANALYSIS DETAILS – 2.5D BEAM

Table B1 Standard deviation of stress and mean stress for all beam nodes as resulting from the respective techniques.

Iteration	Lloyd's Algorithm		PIVOT Treatment A		PIVOT Treatment B	
	St Dev (in MPa)	Mean (in MPa)	St Dev (in MPa)	Mean (in MPa)	St Dev (in MPa)	Mean (in MPa)
0	133.18	142.83	133.18	142.83	133.18	142.83
1	124.70	135.90	136.39	156.50	116.80	126.74
2	122.09	135.00	138.33	163.79	109.74	116.01
3	121.80	136.44	138.12	166.94	104.37	109.91
4	122.10	138.88	138.01	169.25	101.66	108.95
5	120.62	141.92	137.16	170.58	100.42	108.15
6	120.22	144.41	136.14	171.68	99.63	107.74
7	119.53	146.25	136.52	173.53	102.53	106.94
8	120.07	148.27	137.04	175.52	103.43	108.06
9	120.89	150.07	136.38	176.10	100.89	104.98
10	122.08	150.98	138.49	178.12	101.43	104.94
11	122.37	152.17	138.24	177.08	101.86	102.47
12	122.69	153.29	139.30	179.50	103.62	103.78
13	123.92	153.66	138.86	177.89	106.98	108.58
14	123.77	153.40	139.22	176.95	100.39	102.33
15	124.23	154.35	139.83	178.48	102.07	103.92
16	124.39	154.73	139.31	177.37	103.02	103.86
17	124.56	154.91	139.62	177.43	101.88	103.67
18	124.10	154.70	139.09	175.03	98.54	101.97
19	123.73	154.59	140.84	177.63	102.53	104.98
20	123.81	154.60	141.50	178.75	99.92	103.61

Table B2 Maximum stress and total strain energy of the beam obtained by the respective techniques.

Iteration	Lloyd's Algorithm		PIVOT Treatment A		PIVOT Treatment B	
	Max Stress (in MPa)	Total Strain Energy (in mJ)	Max Stress (in MPa)	Total Strain Energy (in mJ)	Max Stress (in MPa)	Total Strain Energy (in mJ)
0	1791.90	12.97	1791.90	12.97	1791.90	12.97
1	1463.40	12.48	1629.20	14.58	1287.90	11.26
2	1429.40	12.39	1412.80	15.34	1202.80	10.10
3	1488.10	12.51	1506.40	15.83	1017.50	9.31
4	1413.70	12.74	1401.90	16.06	923.50	9.10
5	1413.00	13.04	1586.80	16.30	882.57	8.83
6	1409.80	13.34	1526.00	16.61	771.39	8.70
7	1294.70	13.60	1525.70	16.83	923.98	8.74
8	1284.90	13.82	1468.50	17.19	684.15	8.88
9	1442.60	14.02	1274.10	17.29	698.86	8.39
10	1417.20	14.15	1462.80	17.75	651.41	8.62
11	1434.60	14.26	1422.70	17.60	709.84	8.45
12	1410.10	14.33	1266.40	18.02	782.30	8.72
13	1520.10	14.41	1256.00	17.81	894.53	9.20
14	1519.70	14.46	1243.50	17.76	681.28	8.42
15	1513.90	14.52	1297.10	17.85	638.04	8.53
16	1507.30	14.56	1238.50	17.75	793.24	8.68
17	1493.40	14.58	1261.30	17.80	814.35	8.72
18	1478.80	14.59	1225.00	17.53	642.84	8.45
19	1468.20	14.61	1270.60	17.87	822.12	8.69
20	1446.50	14.63	1339.40	18.00	653.59	8.56

Table B3 Standard deviation of stress and mean stress for the inner beam nodes as resulting from the respective techniques.

Iteration	Lloyd's Algorithm		PIVOT Treatment A		PIVOT Treatment B	
	St Dev (in MPa)	Mean (in MPa)	St Dev (in MPa)	Mean (in MPa)	St Dev (in MPa)	Mean (in MPa)
0	69.76	107.40	69.76	107.40	69.76	107.40
1	69.23	108.74	83.19	123.50	63.10	99.64
2	71.11	109.84	83.57	124.69	59.68	89.15
3	70.65	113.94	85.51	128.79	56.62	83.34
4	72.94	118.02	84.92	131.16	55.64	83.09
5	72.27	122.10	84.84	135.98	56.05	79.04
6	73.42	125.73	85.88	140.46	58.32	82.90
7	75.12	130.94	88.52	145.39	54.33	77.93
8	75.86	134.33	88.95	146.33	57.53	83.91
9	78.51	138.10	92.69	150.04	53.46	79.18
10	78.76	137.69	97.14	154.95	53.61	78.59
11	79.44	138.89	95.50	153.39	55.67	80.16
12	80.24	139.40	97.68	156.19	53.76	76.45
13	79.83	139.61	95.38	153.40	57.86	80.94
14	78.12	138.16	95.50	150.25	49.78	70.65
15	79.58	139.42	94.22	152.18	44.60	71.88
16	79.86	138.80	91.23	148.89	52.69	71.59
17	79.34	138.70	95.37	152.62	48.51	73.36
18	79.30	138.83	91.30	147.57	52.53	74.74
19	79.95	138.97	93.40	149.79	43.62	70.23
20	79.90	139.15	96.41	152.64	48.45	71.90

APPENDIX C

STRUCTURAL ANALYSIS DETAILS – 3D BEAM

Table C1 Detailed summary from structural analysis of Case I.

Parameter	Iteration	Lloyd's Algorithm	PIVOT Treatment A	PIVOT Treatment B
Standard Deviation of Stress (in MPa)	0	28.82	28.82	28.82
	1	30.03	30.52	29.20
	2	29.81	30.23	27.96
	3	29.69	30.63	25.30
	4	29.60	30.95	23.94
	5	29.59	31.38	23.36
	6	29.50	31.36	23.25
	7	29.47	31.55	22.85
	8	29.23	31.89	23.23
	9	29.22	32.09	23.03
Mean Stress (in MPa)	0	30.03	30.03	30.03
	1	31.16	33.48	29.55
	2	30.86	33.83	28.06
	3	30.50	34.37	26.49
	4	30.29	34.61	26.04
	5	30.02	34.98	26.40
	6	29.72	35.16	27.01
	7	29.55	35.38	26.75
	8	29.34	35.70	27.06
	9	29.22	35.89	26.94
Maximum Stress (in MPa)	0	316.84	316.84	316.84
	1	374.24	372.19	387.75
	2	371.18	356.52	335.48
	3	364.22	348.33	293.10
	4	322.51	338.40	239.65
	5	343.92	360.74	254.91
	6	345.74	312.75	192.87
	7	351.39	325.96	188.76
	8	325.08	303.65	221.44
	9	335.07	308.29	229.80

Table C2 Detailed summary from structural analysis of Case II.

Parameter	Iteration	Lloyd's Algorithm	PIVOT Treatment A	PIVOT Treatment B
Standard Deviation of Stress (in MPa)	0	23.82	23.82	23.82
	1	25.71	26.38	25.36
	2	26.68	27.88	25.16
	3	26.94	28.08	23.29
	4	27.25	28.25	22.56
	5	27.85	28.18	22.41
	6	28.09	28.57	22.12
	7	27.65	28.79	22.33
	8	27.70	28.98	22.65
	9	27.36	29.20	22.57
Mean Stress (in MPa)	0	27.18	27.18	27.18
	1	27.62	28.78	26.93
	2	28.01	30.19	26.92
	3	27.90	30.85	26.05
	4	27.95	31.15	25.36
	5	28.28	30.98	25.07
	6	28.38	31.25	24.55
	7	28.26	31.39	24.54
	8	28.46	31.41	24.61
	9	28.12	31.56	24.63
Maximum Stress (in MPa)	0	235.99	235.99	235.99
	1	260.01	303.47	226.23
	2	293.91	343.31	256.05
	3	257.73	320.39	222.22
	4	261.85	261.21	219.99
	5	326.48	258.34	197.19
	6	338.42	283.56	202.21
	7	283.53	303.58	196.37
	8	305.67	299.44	216.44
	9	316.94	300.62	205.91

Table C3 Detailed summary from structural analysis of Case III.

Parameter	Iteration	Lloyd's Algorithm	PIVOT Treatment A	PIVOT Treatment B
Standard Deviation of Stress (in MPa)	0	27.05	27.05	27.05
	1	28.64	29.07	27.30
	2	28.81	29.39	27.46
	3	29.05	29.76	26.28
	4	29.26	29.88	25.23
	5	29.31	30.18	23.95
	6	29.33	30.40	23.84
	7	29.20	31.58	23.51
	8	29.15	30.86	23.55
	9	28.76	30.66	23.13
Mean Stress (in MPa)	0	29.51	29.51	29.51
	1	30.76	32.40	29.04
	2	30.70	32.68	29.98
	3	30.70	33.14	29.12
	4	30.98	33.59	28.70
	5	30.73	33.83	27.47
	6	30.73	34.06	27.26
	7	30.60	34.90	26.71
	8	30.46	34.01	26.48
	9	29.96	34.11	26.10
Maximum Stress (in MPa)	0	301.38	301.38	301.38
	1	316.43	304.32	319.93
	2	290.52	332.63	289.25
	3	304.18	283.57	299.00
	4	323.69	286.71	229.46
	5	347.69	285.33	210.23
	6	360.96	279.47	208.20
	7	371.63	327.88	224.50
	8	357.92	298.79	269.72
	9	367.94	280.86	209.18

Table C4 Detailed summary of the total strain energy.

Parameter	Iteration	Lloyd's Algorithm	PIVOT Treatment A	PIVOT Treatment B
Total Strain Energy (mJ) for Case I	0	3.14	3.14	3.14
	1	3.40	3.66	3.23
	2	3.39	3.71	2.94
	3	3.36	3.78	2.69
	4	3.33	3.79	2.57
	5	3.29	3.84	2.50
	6	3.26	3.89	2.55
	7	3.22	3.92	2.52
	8	3.18	3.98	2.56
	9	3.16	4.03	2.56
Total Strain Energy (mJ) for Case II	0	2.57	2.57	2.57
	1	2.81	2.99	2.70
	2	2.91	3.24	2.65
	3	2.95	3.32	2.51
	4	2.97	3.36	2.39
	5	2.99	3.37	2.36
	6	2.99	3.39	2.32
	7	2.99	3.41	2.34
	8	2.99	3.40	2.33
	9	3.00	3.42	2.31
Total Strain Energy (mJ) for Case III	0	3.02	3.02	3.02
	1	3.24	3.45	2.96
	2	3.28	3.50	3.05
	3	3.28	3.55	2.96
	4	3.26	3.58	2.80
	5	3.24	3.61	2.64
	6	3.23	3.61	2.62
	7	3.20	3.64	2.59
	8	3.17	3.65	2.53
	9	3.12	3.65	2.50